Editors' Suggestion

Quantum Chemistry Treatment of Silicon-Hydrogen Bond Rupture by Nonequilibrium Carriers in Semiconductor Devices

Markus Jech,[1,*] Al-Moatasem El-Sayed,[1,2,†] Stanislav Tyaginov,[3,1,4,‡] Dominic Waldhör,[1,§] Foudhil Bouakline,[5,¶] Peter Saalfrank,[5,‖] Dominic Jabs,[6,**] Christoph Jungemann,[6,††] Michael Waltl,[1,‡‡] and Tibor Grasser[1,§§]

[1] *Institute for Microelectronics, Technische Universität Wien, Vienna A-1040, Austria*
[2] *Nanolayers Research Computing Ltd., 1 Granville Court, Granville Road, London N12 0HL, United Kingdom*
[3] *imec, Kapeldreef 75, Leuven B-3001, Belgium*
[4] *Ioffe Institute, St. Petersburg 194021, Russia*
[5] *Institut für Chemie, Universität Potsdam, Potsdam-Golm D-14476, Germany*
[6] *Institut für Theoretische Elektrotechnik, RWTH Aachen University, Aachen D-52062, Germany*

(Received 12 April 2021; accepted 3 June 2021; published 9 July 2021)

The interaction of charge carriers with hydrogen-related defects plays a key role in modern semiconductor applications. Particularly in the field of micro- and nanoelectronics, where silicon together with amorphous gate oxides is still the technology of choice, Si—H bonds participate in a rich variety of phenomena. For example, the passivating nature of H and its influence on surface reconstruction are fundamentally useful features for modern technologies and emerging research fields alike. However, the dissociation of Si—H bonds results in electrically active defects and is associated with a number of device reliability issues. In this work we develop a general quantum kinetic formulation to describe the dynamics of bond excitation and breaking. The wealth of experimental and theoretical studies on Si—H bond breaking induced by energetic carriers enables us to extract the most useful excitation pathways. Based on the open-system density-matrix theory we develop a model that accounts for all relevant system-bath interactions: vibrational relaxation and dipole scattering as well as resonance-induced excitation. In contrast to existing theoretical studies, our model is coupled to a Boltzmann transport equation solver, which is required for the correct consideration of nonequilibrium carrier energy distribution functions occuring in an electronic device. Finally, we apply our framework to model Si—H bond breakage at the Si/SiO_2 interface and validate our approach against different experimental data sets. The results provide a fundamental understanding of Si—H dissociation mechanisms and allow for an accurate microscopic description of hot-carrier-induced damage at the device level. Due to the model formulation being free of empirical parameters, the approach can be easily applied to future technologies and materials systems.

DOI: 10.1103/PhysRevApplied.16.014026

I. INTRODUCTION

Material defects are unavoidable in any electronic device and their existence is a major challenge for nanoscale electronics that impose limits on their reliability. Point defects induced during processing or generated during operation potentially act as localized trapping sites for charges and thereby strongly affect the electrical performance. Among the various degradation phenomena, bias temperature instabilities (BTI) [1–4] and hot-carrier degradation (HCD) [5–9] are the main concerns in modern MOSFETs, as recently reported by Intel [10]. While the theory of BTI is already quite well understood within the framework of nonradiative multiphonon transitions [11], the underlying physics of HCD have not been fully clarified yet.

During hot-carrier degradation, hydrogen-passivated silicon bonds at the Si/SiO_2 interface are broken and silicon dangling bonds (DBs) are created, which are commonly referred to as P_b centers [12]. These amphoteric dangling bonds exhibit two trap levels within the silicon band

*jech@iue.tuwien.ac.at
†elsayed@iue.tuwien.ac.at
‡stanislav.tyaginov@imec.be
§waldhoer@iue.tuwien.ac.at
¶bouakline@uni-potsdam.de
‖peter.saalfrank@uni-potsdam.de
**dj@ithe.rwth-aachen.de
††cj@ithe.rwth-aachen.de
‡‡waltl@iue.tuwien.ac.at
§§grasser@iue.tuwien.ac.at

 © 2021 American Physical Society

gap and are electrically active [13–16]. Depending on the Fermi level inside the semiconductor, the DB becomes charged and locally perturbs the electrostatics of the device and degrades the carrier mobility. A feature of HCD is its strong spatial localization. The largest number of Si DBs, and thus the largest damage, is always observed close to the drain end of the channel. To describe this phenomenon, HCD models have evolved from phenomenological approaches [17,18] to more complex formulations to capture its manifold dependencies [5,7,19].

The major breakthrough in modeling and understanding HCD in electronic devices is due to the work by the group of Hess [20–23]. This work also serves as a basis for further developments by two groups, namely the group of Bravaix [8,9] and our own work [6,24]. The key idea and overall assumptions of these models is to link a thorough carrier-transport treatment with two different but interacting regimes for defect creation: a direct and an indirect excitation mechanism of the Si—H bond.

While carriers move through the channel of a MOSFET, they can undergo different scattering events, thereby exchanging energy, which results in a rather broad and complex distribution of energies, including a high energy tail, i.e., *heated* carriers. The quantity that, therefore, needs to be addressed is the carrier energy distribution function (EDF). The EDF is a continuous quantity, which provides information on how carriers are distributed over energy. Consequently, an adequate description of carrier transport is compulsory for a proper treatment of hot-carrier-related reliability issues in semiconductor devices.

The actual defect creation mechanism is dominated by two regimes, namely a single-particle (SP) and a multiple-particle (MP) mechanism. The SP process accounts for the high-energy fraction of the carrier ensemble in the channel. Only one solitary carrier, with an energy greater than the excitation threshold of this process, triggers the desorption of hydrogen. This regime is based on the physical context of an electronic excitation of one of the valence electrons. On the other hand, the MP mechanism describes a consecutive ladder climbing process. Several carriers with moderate energies are needed to excite the vibrational eigenstates of the Si—H bond. However, no details of the physical principle of vibrational excitation of the bond by channel carriers has so far been given, despite its relevance in recent modeling approaches. While the group of Hess [23] has speculated about a resonance-based process, this idea has never been implemented in an actual model. The basic idea here is that electrons possibly localize in the vicinity of the Si—H bond via an accessible electronic resonance state and can excite its phonon modes.

This paper aims at developing a consistent physical model, which describes how carriers with energies following a nonequilibrium distribution function interact and eventually break a silicon hydrogen bond. Preliminary results and a superficial outline of the established framework have been published in a recent work [25]. However, this work presents a complete bottom-up approach ranging from atomistic details explored using classical force fields and density-functional theory (DFT) to a description of a quantum-mechanical model for bond dissociation up to semiconductor device simulations, including carrier transport. We focus on the various possible physical origins of Si—H bond-breaking mechanisms and develop a model for describing its dynamics, which can be applied to capture hot-carrier degradation at the device level. Our model is based on a large number of experimental and theoretical studies, offering a wealth of information explaining the interaction of electrons and adsorbates on surfaces. In particular, we use scanning tunneling microscope studies and combine these results with our own data to identify the responsible processes triggered by *hot carriers* in a device, see Sec. II. In Sec. III we provide details about the theoretical concepts being utilized. We use the *density-matrix formalism for an open quantum system* to capture the dynamics of the Si—H bond when interacting with its environment. The bond-breakage trajectory is an essential ingredient, which has been identified in our recent work, see Ref. [26]. Subsequently, we develop a model to explain hot-carrier-induced damage at the Si/SiO_2 interface and apply the framework to describe different measurement trends, see Sec. IV. Finally, we discuss how our approach improves the understanding of the interaction with different charge carriers, electrons and holes, and the implications on electronic devices and future technologies.

II. EXPERIMENTALLY INDUCED EXCITATION MECHANISMS

Due to the technological relevance of the silicon surface for the majority of nanoelectronic devices, its various surface orientations have already been very well examined. Controlling and dissociating single adsorbates on a surface is a key step towards understanding the dynamics of bond breaking. Popular methods to excite and/or desorb the surface-adsorbate complex include the STM and lasers (using either infrared or ultraviolet photons). While STM experiments use electrons to excite and desorb individual molecules and adsorbates, lasers can trigger dissociation or excitation either directly or indirectly: in the direct case photons couple to the complex's transition dipole moment, whereas the indirect route has been found to be substrate mediated via a resonance [27].

As discussed in the Introduction, breaking of Si—H bonds plays a major role for device reliability issues, specifically for HCD at the Si/SiO_2 interface. In agreement with investigations on Si dangling bonds on surfaces, the same kinds of defects are also present in electronic devices, known as P_b centers. The technologically relevant $(100)Si/SiO_2$ interface exhibits two defects called P_{b0}

and P_{b1}, with their symmetry axis not aligned with the surface normal [13–15,28–30]. Both defects have been clearly identified using ESR spectroscopy as a single sp^3 hybrid orbital facing a silicon atom vacancy. However, only the P_{b0} was clearly associated with a trivalent interfacial Si back bonded to three Si atoms in the bulk [13,28]. The properties of the P_{b1} center, on the other hand, are quite controversial and different groups have suggested contradictory atomistic structures [15,31–33]. However, the overall characteristics of interface defects—ESR response, amphoteric character with defect levels inside the silicon band gap, and its atomistic structure—render them compatible to DBs observed at terminated Si surfaces [34,35].

Reviewing the wealth of information available for H dissociation on a passivated Si surface suggests that the various excitation mechanisms can be separated to extract the most useful contributions. By comparing the requirements to trigger specific bond-breaking mechanisms to the conditions in a MOSFET, it is possible to link the well-known desorption induced by electronic transition (DIET) and desorption induced by multiple electronic transition (DIMET) processes [27,36,37] to possible excitations in electronic devices. Note that in the following experiments breaking a single Si—H bond on the surface is dominated by its stretching mode [38,39]. While the energetic situation and the dissociation mechanism in a MOSFET is certainly different compared to STM measurements as we have shown in a recent study, see Ref. [26], we demonstrate that the physical principle of how carriers interact with bonds and trigger excitations is consistent with the aforementioned studies, see Fig. 1.

A. Electronic excitations

A significant contribution towards the understanding of STM-induced Si—H bond breaking was made by the group of Avouris [40–42], who suggested that one possible way to trigger H dissociation is related to an electronic excitation. An excited electronic state can be formed on an

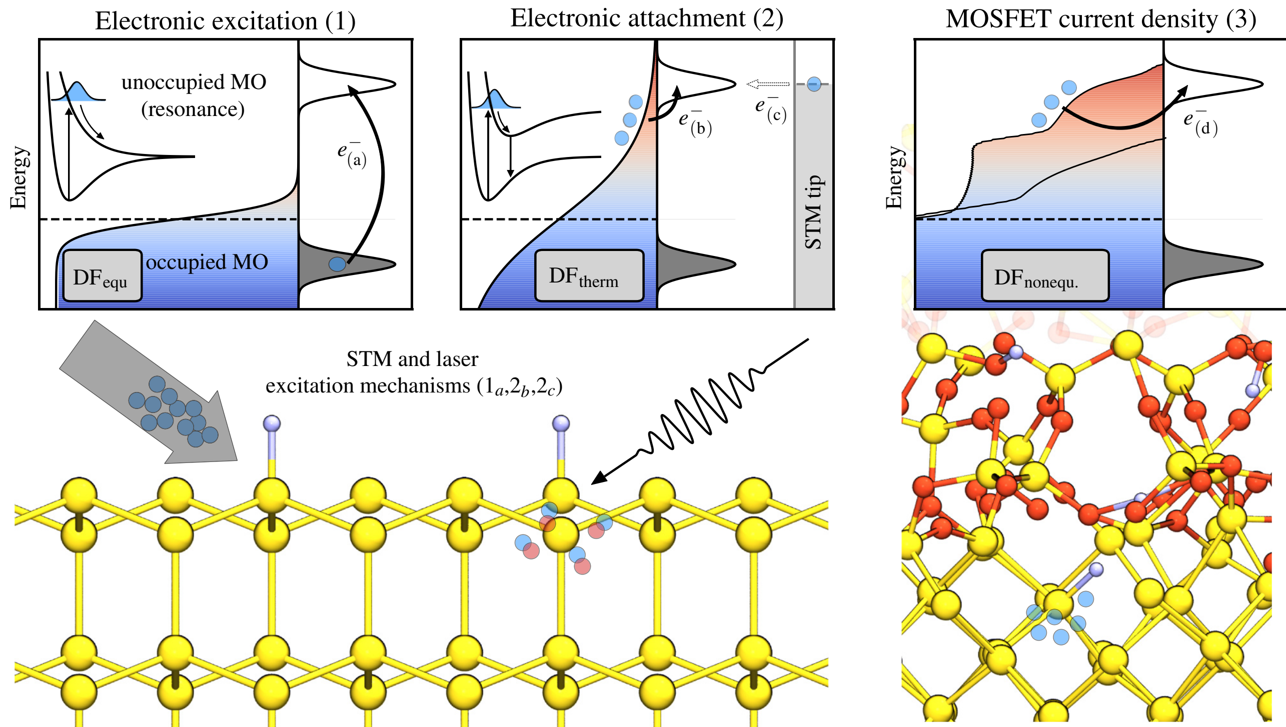

FIG. 1. Schematics of possible electronic excitation processes (lower panels) together with their energetics (upper panels). (1a) Electronic excitation of one of the bonding electrons to an antibonding orbital of the Si—H bond on a silicon surface. Provided that the created excited state exhibits a repulsive potential, bond breaking can be induced. Such a process can be triggered by electrons emitted by a STM tip or photons from a laser light with sufficient energy. (2b) Substrate-mediated photochemistry on a surface. The incident photon creates a thermalized distribution (described by a Fermi-Dirac distribution) and carriers can scatter into an unoccupied state. (2c) STM-induced excitation of a Si—H bond via electron attachment. The carriers can tunnel into an adsorbate-induced resonance and upon inelastic relaxation produce multiple vibrational excitations. By applying a voltage on the surface with respect to the tip one can adjust the energies of the tunneling electrons. (3d) Charge carriers with distributed energies supplied by a current flowing through a MOSFET. The carriers are accelerated by the electric field and undergo various scattering events, which results in a complex distribution function (note that the superimposed distribution function is shown on a logarithmic scale), severely distorted from the equilibrium. If carriers gain enough energy they can scatter into a resonance, similar to (2b),(2c).

adsorbate complex when the electron energy in the STM exceeds the threshold of one of the possible electronic transitions, see Fig 1 (1). Provided that the newly created state is sufficiently repulsive, breaking of adsorbate-surface bonds can be induced. In the case of Si—H bonds, this excitation is associated with a $\sigma \rightarrow \sigma^*$ transition (σ, occupied bonding orbital; σ^*, unoccupied antibonding orbital), thereby changing the potential energy profile to a repulsive potential. Such a mechanism for Si—H bond breaking has been suggested in many papers [36,43–52] with an onset of approximately 6.5 eV and a peak at 8 eV. Experimentally it was found that increasing the energy of the STM electrons beyond this value did not impact the hydrogen desorption yield. Comparable results have been reported using laser light (157 nm, 7.9 eV) to trigger direct photodesorption of atomic hydrogen from Si surfaces [53–55]. Additionally, theoretical studies [40,56] showed that a competing effect of motion on the excited potential is electronic quenching, which will relax the system back to its electronic ground state. This efficient mechanism results in hydrogen desorption originating from a rather *hot* ground state, i.e., a vibrationally excited ground state, than from the excited potential profile.

B. Multiple-vibrational excitations

When the sample bias of the STM is reduced below the threshold of the electronic excitation, it has been observed that the yield is lower but not zero [38,43,57]. Furthermore, the yield in the energy range between 2 and 6 eV strongly depends on the applied voltage and the tunneling current [37–39,57,58]. The underlying mechanism is due to tunneling electrons resonantly scattering at the adsorbate, see Fig. 1 (2), thereby triggering vibrational excitations [38,40,57]. In the case of the Si—H bond it is assumed that the unoccupied σ^* orbital is associated with this process [38,57]. The same mechanism applies to holes scattering into an available cation resonance formed by the occupied σ orbital of the Si—H complex.

Although the measurement data reported by various groups [38,40,43,57] could be explained quite well by different vibrational heating models, using either a coherent or an incoherent formulation, the details of the mechanism are not yet fully understood. In both models an electron attaches to an unoccupied orbital, thereby forming a negative ion resonance. During the inelastic relaxation process of the electron, it transfers a part of its energy to the Si—H vibration. While in the incoherent formulation it is only able to transfer one quantum of energy, the coherent model allows for a bigger portion and thus enables the electron to excite a larger number of vibrational quanta. However, in more recent publications [57,59] it was shown that less electrons are needed to dissociate hydrogen than assumed in the incoherent model. This renders the coherent formulation more compatible to the observed behavior.

C. Dipole-induced excitations

Another excitation channel is related to the interaction of the vibrational transition dipole of an adsorbate with an electric field [60]. The electric field due to the electrons' tunneling from the STM tip to the surface is able to couple to the transition dipole moment and induce a transition between vibrational states. Examining an adsorbate on a surface with a STM, the dominant dipole component is perpendicular to the surface, which corresponds to the directions of the tunneling electrons.

D. Relation to HCD

The detailed picture of excitation processes together with the understanding of how charge carriers can interact with an adsorbate complex presented in this section provides the fundamental framework to describe hot-carrier-related degradation phenomena in MOSFETs. There is an unambiguous connection between experimentally observed Si—H bond-breaking processes and HCD in electronic devices, see Fig. 1 (3). One possibility to dissociate H is clearly associated with an electronic excitation, namely the $\sigma \rightarrow \sigma^*$ transition. However, rather high energetic carriers, which are unlikely to be present in an electronic device, of about 6–8 eV are needed to trigger such an electronic transition. On the other hand, a combination of an electronic (anionic and cationic) resonance scattering and vibrational heating mechanism seems more likely to be the driving force for the creation of interface states, see Fig. 1 (2) and (3). The moderate carrier energies needed for this excitation channel together with its strong current dependence agree well with the characteristic features of hot-carrier effects in MOSFETs. However, dipole-induced excitations are more complicated to quantify. First, the Si—H bond at the Si/SiO_2 interface is generally not perpendicular to the interface, but rather forms an angle of approximately 54.7° with respect to the Si(100) surface normal in its idealized configuration. Furthermore, charged carriers move parallel to the interface in the inversion layer of the MOSFET, which results in a more complex coupling to the Si—H dipole moment, which is given by $\mathbf{E} \cdot \boldsymbol{\mu}$, where $\mathbf{E}$ is the electric field and $\boldsymbol{\mu}$ is the dipole moment vector. Second, additional spatial-dependent fields are present in an electronic device during operation. However, as we show in Appendix D, the Si—H bond exhibits only a small dipole vector and interacts extremely weakly with moderate electric field strengths. Thus, we expect a very small contribution from this excitation mechanism.

III. MODELING FRAMEWORK

This part of the paper focuses on the theoretical foundations, namely an adequate description of carrier transport in electronic devices, the formulation of the transition rates

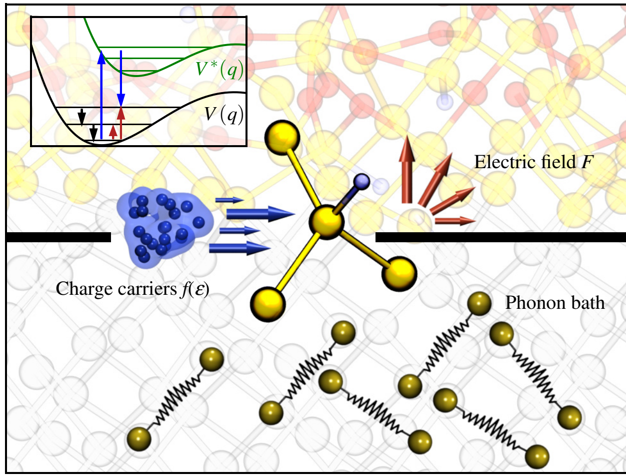

FIG. 2. Schematic visualization of the different interactions considered in this work. The dynamics of a Si—H bond at the silicon-oxide interface are determined by inelastic scattering due to electrons, namely dipole- and resonance-induced excitations, characterized by the EDF $f(\epsilon)$ and relaxation due to the coupling with the phonon bath. The excitation and eventually breakage of the Si—H complex proceeds via an anion or cation resonance state $V^*(q)$, where q is the reaction coordinate.

$\Gamma_{i,f}$ between vibrational eigenstates of the Si—H bond, and the relation of such a microscopic description to the experimentally quantifiable degradation trend. The aim is to capture the fundamental physics behind the interaction of Si—H bonds at the Si/SiO_2 interface with its environment including energetic charge carriers.

As already outlined in the previous section there are three major contributions that determine the dynamics of the Si—H bond:

(a) Vibrational dipole-induced excitations triggered by a current.

(b) Excitations due to a transient population of an electronic resonance state.

(c) Vibrational relaxations according to the coupling with the surrounding phonon bath.

While the first two components can be formulated in terms of an inelastic scattering process of an incoming carrier and strongly depend on the density of charge carriers and their distribution over energy, the latter requires knowledge of the environment and its properties. A graphical illustration of the individual processes is schematically given in Fig. 2. Each component and ingredient of the proposed approach will be discussed in detail below.

A. Device simulations

Modern-technology computer-aided design (TCAD) has become a powerful tool for the development of semiconductor devices and technologies. Despite inevitable deficiencies for ultrascaled devices, which can only be rectified using empirical arguments, moment-based approaches such as the drift diffusion or the hydrodynamic scheme [61] are still among the most popular simulation methods. However, for particular applications, such as hot-carrier-related device reliability issues, a deeper understanding of the underlying physical processes together with an adequate description of carrier transport at the nanometer scale is mandatory [62,63].

The Boltzmann transport equation (BTE), obeying semiclassical dynamics for electrons together with a quantum-mechanical treatment of scattering, is commonly considered to provide an accurate description for the continuous carrier probability distribution function $f(\mathbf{x}, \mathbf{k}, t)$. The latter is a seven–dimensional quantity depending on time t, the spatial coordinate $\mathbf{x}$ and momentum space $\mathbf{k}$. The BTE is given by

$$\left(\frac{\partial}{\partial t} + \mathbf{v} \cdot \nabla_{\mathbf{x}} + \frac{\mathbf{F}}{\hbar} \cdot \nabla_{\mathbf{k}}\right) f(\mathbf{x}, \mathbf{k}, t) = Q\{f(\mathbf{x}, \mathbf{k}, t)\}, \quad (1)$$

where $\mathbf{v}$ is the carrier velocity depending on the carrier momentum, $\mathbf{F}$ denotes the electrostatic force due to the particle charge obtained through a self-consistent solution of the Poisson equation, and Q refers to the scattering operator. However, solving the BTE, in particular obtaining a self-consistently coupled solution for electrons and holes, f_n and f_p, is a computationally challenging task due to the high dimensionality of the problem. Two different approaches have been established in the past to numerically solve the BTE: a stochastic formulation using the Monte Carlo method [65], and a deterministic approach employing the spherical harmonic expansion (SHE) method [66], which has been used in this work. The SHE approach exploits the expansion of the distribution of carrier momentum into spherical harmonics

$$f(\mathbf{x}, \mathbf{k}, t) = \sum_{l=0}^{\infty} \sum_{m=-l}^{l} f_{l,m}(\mathbf{x}, \varepsilon, t) Y^{l,m}(\theta, \varphi), \quad (2)$$

where the wave vector $\mathbf{k}$ is written in spherical coordinates ε, θ, and φ on equienergy surfaces. For mathematical details and derivations the reader is referred to the literature, see Refs. [67–69], and in particular to Ref. [66] for recent computational advances.

Within this work we consider several types of carrier interactions with the crystal lattice or with other carriers, represented by the scattering operator $Q\{f(\mathbf{x}, \mathbf{k}, t)\}$ in Eq. (1). The scattering operator is assumed to be given in the linear form [66,67,70]

$$Q\{f(\mathbf{x}, \mathbf{k}, t)\} = \frac{1}{(2\pi)^3} \int_{\mathcal{B}} s(\mathbf{x}, \mathbf{k}', \mathbf{k}) f(\mathbf{x}, \mathbf{k}', t) - s(\mathbf{x}, \mathbf{k}, \mathbf{k}') f(\mathbf{x}, \mathbf{k}, t) d\mathbf{k}', \quad (3)$$

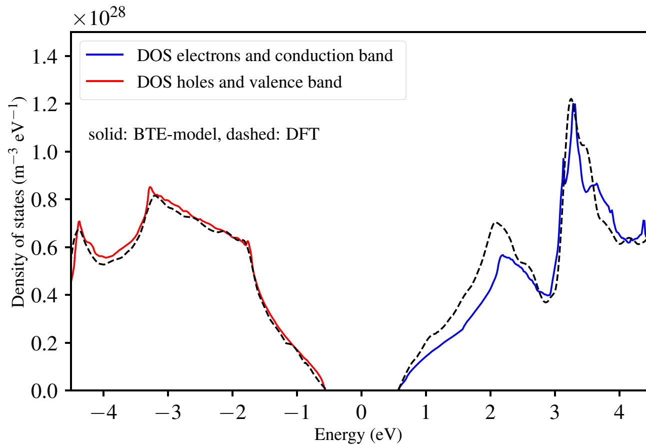

FIG. 3. Density of states for Si when considering full band effects as done in the Boltzmann transport equation according to the formulation in Ref. [64]. Shown are the density of states for the conduction and valence band for silicon as used in our approach, which nicely reproduces the DOS of the full band structure obtained from DFT calculations for the full energy range.

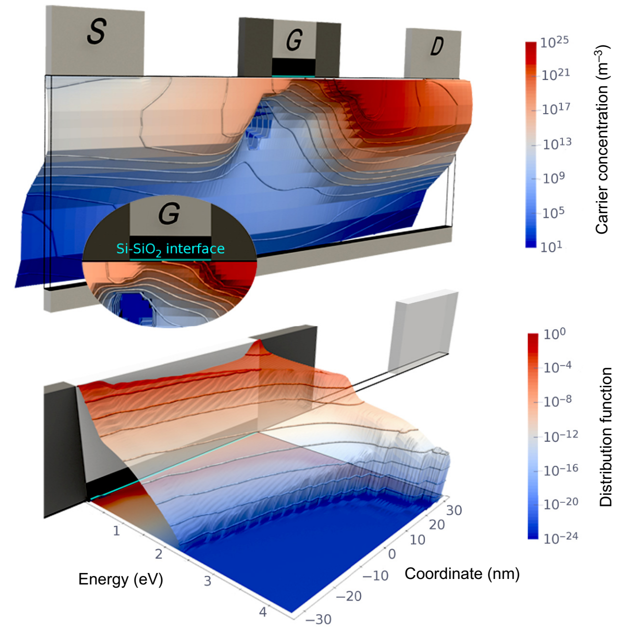

FIG. 4. A solution of the Boltzmann transport equation of a 65-nm SiON-based nMOSFET calculated at the bias conditions $V_G = V_D = 2.2$ (V) and $T = 293$ K with our deterministic Boltzmann transport equation solver. The upper panel shows the distribution of carriers with energies higher than 1 eV. Clearly visible is the accumulation of hot carriers at the drain end of the channel due to the acceleration of carriers induced by the electric field along the channel-oxide interface. The complete energy distribution function along the Si/SiO$_2$ interface is given in the lower panel. Due to the electrostatic force and the various scattering mechanisms, the EDF evolves from a Fermi-Dirac-like distribution in equilibrium on the source side to a complex EDF including a heated carrier ensemble towards the drain.

with $s(\mathbf{x}, \mathbf{k}, \mathbf{k}')$ being the rate of transition from $\mathbf{k}$ to $\mathbf{k}'$ in phase space. Particle interactions such as (approximately) elastic and inelastic events due to acoustic and optical phonon scattering, surface scattering, scattering at ionized impurities, as well as impact ionization have been included in the present calculations. Furthermore, full band effects, based on the proposed method in Ref. [64], are included in our simulations due to the occurrence of carriers with substantial energies, which can not be adequately described within simplified approaches, which describe only the band structure near the valence- and conduction-band edge properly. The utilized formulation for the density of states for the conduction and valence band is shown in Fig. 3 and compared to a bulk silicon DFT calculation conducted with the CP2K package in conjunction with the semilocal Perdew-Burke-Ernzerhof (PBE) functional. Further technical details can be found in the Appendix.

The procedure to couple the device simulations of the MOSFETs to the calculations for the creation of interface defects using the solutions of the BTE is as follows: first, the device structures are calibrated to measurements of the pristine device using $I_D - V_G$ characteristics within our device simulator Minimos–NT [71,72] employing a drift-diffusion scheme. Subsequently, for selected bias points (the stress conditions for which the degradation has been characterized) a full self-consistent solution of the BTE for electrons and holes is obtained, which yields the information on how carriers are distributed over energy, given as the energy distribution function. This information is further used within our modeling approach to account for the interaction of *hot* carriers with Si—H bonds at the channel-oxide interface and calculate the bond dynamics, i.e., the number of created interface defects $N_{\mathrm{it}}(t)$. Ultimately, this quantity is coupled back to our TCAD tool to calculate the impact of those defects as a degradation trend over time. An example for a BTE solution is given in Fig. 4, which shows the electron EDF of an nMOSFET calculated at $V_G = V_D = 2.2$ V and $T = 293$ K. The upper graph shows the density of carriers, which possess an energy greater than 1 eV. Clearly visible is the characteristic accumulation of energetic, *hot*, carriers at the drain end of the channel. Carriers gain energy due to the acceleration of the electric field along the channel, but also exchange energy via the aforementioned scattering mechanisms. This results in an evolution of the EDF from source to drain, as can be seen in the lower panel of Fig. 4, and a rather complex shape of the EDF including a high energy tail, which extends up to 4 eV and represents the *heated* carrier ensemble.

B. Theoretical treatment: system-bath interactions

Ideally, all dissipative and inelastic couplings leading to changes of the states in the total system are included. However, due to the macroscopic nature of the *bath*, an explicit

treatment of the *system's* dynamics is desired while the *bath* entity is described implicitly. Here, the term *system* refers to the Si—H complex, while the description of the *bath* or *environment* applies to silicon-oxide interface and its properties. *Open-system density-matrix theory* is used to study the problem at hand, in particular, the Lindblad semigroup functional formulation [73], which is based on a Markov and secular approximation. Within this approach the bath modes are traced out, which results in equations of motion solely for the *system* part. Expressed through the reduced density operator $\hat{\rho}_S$, the *system dynamics* are governed by the Lindblad equation:

$$\frac{\partial}{\partial t}\hat{\rho}_S(t) = \mathcal{L}_S\hat{\rho}_S + \mathcal{L}_D\hat{\rho}_S = -\frac{i}{\hbar}\left[\hat{H}_S, \hat{\rho}_S\right] + \mathcal{L}_D\hat{\rho}_S, \quad (4)$$

where $\mathcal{L}_S$ and $\mathcal{L}_D$ are the system and dissipative superoperator, respectively. Furthermore, utilizing the eigenstate representation of $\hat{\rho}_S$, such as the eigenfunctions $|\phi_n\rangle$ of the *system* Hamiltonian, $\rho_{nm} = \langle\phi_n|\hat{\rho}|\phi_m\rangle$, allows the interpretation of the diagonal elements ρ_{nn} as the level populations P_n and the off-diagonal represents the coherences between two states.

The dissipative superoperator $\mathcal{L}_D$ within this approach is given by

$$\mathcal{L}_D\hat{\rho}_S = \sum_k \left(\hat{C}_k\hat{\rho}_S\hat{C}_k^\dagger - \frac{1}{2}\left[\hat{C}_k^\dagger\hat{C}_k, \hat{\rho}_S\right]_+\right), \quad (5)$$

with $\hat{C}_k$ being the *Lindblad operators*, defining the nature of a specific dissipative channel indexed by k. They account for population transfer between eigenstates of the ground-state potential energy curve (PEC) of the *system* due to vibrational relaxation and inelastic scattering. Together with Eq. (4) the Lindblad form guarantees positive state populations and a conserved norm by mathematical construction. The Lindblad operators can be expressed as

$$\hat{C}_k = \sqrt{\Gamma_{i,f}}\,|\phi_f\rangle\langle\phi_i|, \quad (6)$$

with $\Gamma_{i,f}$ being the transition rate from the system eigenstate $|\phi_i\rangle$ to the system eigenstate $|\phi_f\rangle$. The transition rate depends on the type of perturbation as well as on the bond complex and its properties. A general formulation is given by Fermi's golden rule (FGR)

$$\Gamma_{i,f} = \frac{2\pi}{\hbar}\sum_{I,F} f_I(T,\epsilon)\,[1 - f_F(T,\epsilon)] \times |\langle\Phi_{F,f}|\hat{V}|\Phi_{I,i}\rangle|^2\delta(E_{I,i} - E_{F,f}), \quad (7)$$

where the summations run over all collective initial I and final states F of the environment, weighted with a probability distribution function $f(T,\epsilon)$. Assuming a weak coupling of the *system* and its *environment*, one can choose $\Phi_{I,i}$ and $\Phi_{F,f}$ to be a product of vibrational system modes $\phi_{i,f}$ and environment states $\Psi_{I,F}$. Depending on the nature of the perturbation, specified by the coupling operator $\hat{V}$, $\Psi_{I,F}$ describes the phonon bath modes with $f(T,\epsilon)$ accounting for the thermal population of the bath oscillator states, whereas for the interaction of a charge carrier with an electronic resonance it describes the electronic subspace for incoming carrier scattering from I to F represented by an energy distribution function $f(T,\epsilon)$.

In the following, Eq. (7) is used to calculate transfer rates of localized Si—H eigenstates due to various mechanisms. Contributions originating from bond vibration-phonon coupling as well as from inelastic electron tunneling are included. The latter can either arise due to dipole scattering or resonance scattering. Eventually, the total rate $\Gamma_{i,f}$ is the sum of all individual contributions:

$$\Gamma_{i,f}^{\text{tot}} = \Gamma_{i,f}^{\text{vib}} + \Gamma_{i,f}^{\text{dip,inel}} + \Gamma_{i,f}^{\text{res,inel}}. \quad (8)$$

C. Model potential

Contrary to H-terminated Si surfaces, where the Si—H stretching mode is assumed to be responsible for the creation of Si dangling bonds, we have recently shown that breaking of Si—H at the Si/SiO_2 follows a more complicated trajectory [26]. In an initial step, the hydrogen atom moves towards an adjacent Si atom and subsequently relaxes into the next but one bond-center site. The ground-state PEC $V(q)$ along the one-dimensional reaction coordinate together with the respective atomistic configurations is shown in Fig. 5. Note that throughout this work we use mass-weighted coordinates $x = \mathbf{x}_{\text{cartesian}} \cdot \sqrt{\mathbf{m}}$. Here, $x_{\text{cartesian},i}$ is the spatial displacement of the involved atom i along the reaction path for the Si—H rupture process extracted in Ref. [26], and m_i is the corresponding mass of the individual atom. The collective motion has been restricted to the direct vicinity of the region of interest, see the highlighted atoms in the top panels of Fig. 5, only including displacements passing the threshold of at least 5% of the maximum displacement. Overall, the reaction path and coordinate is dominated by the movement of the hydrogen atom, see Fig. 5. For all practical applications within this work we use an analytic fit to the DFT results of the following form:

$$V(q) = v_4(q+q_0)^4 - v_2(q+q_0)^2 + v_0\sqrt{\frac{v_0}{2v_2}}(q+q_0), \quad (9)$$

which represents an asymmetric double-well potential. The parameters v_0, v_2, and σ are given in the caption of Fig. 5. For the given parameters the ground-state potential has two minima at $q = -3.2\ \text{a}_0\sqrt{\text{m}}$ and $q = 3.0\ \text{a}_0\sqrt{\text{m}}$ with a barrier of 2.7 eV at $q = 0$ and exhibits 32 bound states

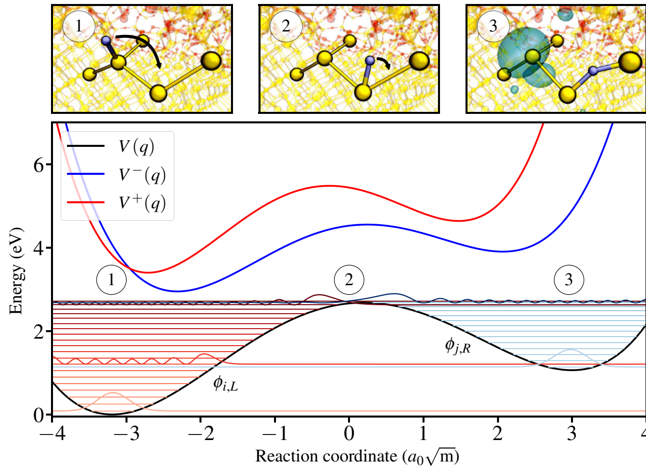

FIG. 5. Model potentials for the ground [$V(q)$] and excited potential energy curves [$V^-(q)/V^+(q)$] along the same reaction coordinate. Selected atomistic configurations for the ground state along the reaction path are shown in the upper panels. The left well corresponds to the initial equilibrium position of the Si—H bond (1), the transition barrier is marked by (2) where the H has moved towards an adjacent Si atom, and the right well (3) describes the final position of the H atom, the next but one bond-center site. The upper three figures show the respective geometries along the reaction path, see Ref. [26]. All PECs are described by the functional form of Eq. (9) with the parameters: $V(q): v_4 = 0.023, v_2 = 0.442, v_0 = 1.062, q_0 = 0$; $V^-(q): v_4 = 0.046, v_2 = 0.459, v_0 = 0.955, q_0 = 0$; $V^+(q): v_4 = 0.072, v_2 = 0.640, v_0 = 1.241, q_0 = 0.5$. All parameters are given in units of eV q^{-2k} for $k = 0, 1, 2$.

(below the barrier), localized either in the left or right well. Selected eigenstates are summarized in Table I.

Additionally, the potential energy curves for the resonance states are also captured by the same functional form, see Eq. (9), as the ground-state PEC. The negatively (positively) charged profile possesses a substantially reduced transition barrier of approximately 1.7 eV (approximately 2.1 eV) and a shifted equilibrium position as shown in Fig. 5. Note that the positive potential $V^+(q)$ additionally exhibits a shifted transition point.

TABLE I. Selected eigenstates for the ground state potential $V(q)$ together with the respective energies and their localization (L/R). Note that the first state localized in the right well is $\phi_{7,R}$.

n	E_n (meV)	n	E_n (meV)
$\phi_{0,L}$	84.44	$\phi_{6,L}$	1054.09
$\phi_{1,L}$	251.98	$\phi_{7,R}$	1138.60
		⋮	⋮
$\phi_{2,L}$	417.25		
$\phi_{3,L}$	580.19	$\phi_{30,L}$	2627.90
⋮	⋮	$\phi_{31,R}$	2675.69

The analytic fits presented here do not aim to provide the most accurate description of the DFT results, but to give a qualitatively correct description of the ground- and excited-state potential energy curves. The primary reason why this approximate treatment is more than sufficient is that due to the amorphous nature of the Si/SiO_2 interface, there is an intrinsic distribution of the parameters such as the transition barrier, minimum position, and the resonance energy. Furthermore, the calculation of electronically excited states is still a difficult challenge even for modern *ab initio* methods, particularly for a Si/SiO_2 interface system. In order to approximate the resonance profiles, $V^-(q)$ and $V^+(q)$, we use two approaches: Koopmans' theorem and the method of constrained density-functional theory (CDFT). Further details can be found in Appendix B.

D. Dissipative transfer

First we consider the basic interaction between the Si—H bond and the substrate to describe the coupling of a bond potential to a *bath* of oscillators. The resulting **vibrational relaxation** rates $\Gamma_{i,f}^{\text{vib}}$, and thus the lifetimes τ_i, determine the dynamics of the bond. As shown above, the reaction coordinate of Si—H breakage at a Si/SiO_2 interface is a combination of the Si—H bending and Si—H stretching modes. Experimental and theoretical studies focused on the vibrational relaxation of the Si—H bond on a *silicon surface* revealed lifetimes on the order of ns and ps for the stretching and bending modes [74–77], respectively. However, for the problem at hand—a mixture of various Si—H modes and a different phonon spectrum—these values can only be used to derive an educated guess for the vibrational relaxation.

Investigating the coupling between the Si—H ground-state fundamental frequency and the substrate in more detail is, therefore, an essential component in our model framework. We employ a perturbation-theory approach together with the classical force-field ReaxFF [78] to calculate the *system-bath* coupling elements and ultimately the transition rates using Fermi's golden rule, see Refs. [75,76,79]. Following Ref. [79], we introduce a new set of coordinates to separate the $3N$-dimensional coordinates $\mathbf{r}$ of the total system into *system* and *bath* degrees of freedom (DOF). The new DOFs $\mathbf{q}$ and $\mathbf{Q}$ are constructed using an orthogonal transformation

$$R_i = \sum_{j=1}^{3N} O_{i,j} r_j, \quad \text{with} \quad \sum_{i=1}^{3N} O_{i,k} O_{i,l} = \delta_{k,l}, \tag{10}$$

where $q_i = R_i (i = 1 \ldots M)$ describe the *system* coordinates and $Q_i = R_i (i = M + 1 \ldots 3N)$ correspond to the *bath* modes. The total Hamiltonian can be decomposed in

the usual *system-bath* form:

$$\hat{H} = \hat{H}_S + \hat{H}_{SB} + \hat{H}_B, \tag{11}$$

with the individual contributions of the *system*, *bath*, and the *system-bath* coupling given by

$$\begin{aligned}
\hat{H}_S &= -\frac{\hbar^2}{2}\sum_{i=1}^{M}\frac{\partial^2}{\partial q_i^2} + V(\mathbf{q},\mathbf{Q}=0),\\
\hat{H}_{SB} &= \sum_{i=1}^{3N-M}\lambda_i(\mathbf{q})Q_i + \frac{1}{2}\sum_{i,j=1}^{3N-M}\Lambda_{i,j}(\mathbf{q})Q_iQ_j,\\
\hat{H}_B &= \sum_{i=1}^{3N-M}\left(-\frac{\hbar^2}{2}\frac{\partial^2}{\partial Q_i^2} + \frac{1}{2}\omega_i^2 Q_i^2\right).
\end{aligned} \tag{12}$$

The one- (linear) and two-phonon (quadratic) coupling functions $\lambda_i(\mathbf{q})$ and $\Lambda_{i,j}(\mathbf{q})$ (corresponding to one- and two-phonon relaxations) can be obtained by calculating the derivative of $V(\mathbf{q},\mathbf{Q})$ as

$$\begin{aligned}
\lambda_i(\mathbf{q}) &= \frac{\partial V}{\partial Q_i}\Big|_{\mathbf{q},\mathbf{Q}=0},\\
\Lambda_{i,j}(\mathbf{q}) &= \frac{\partial^2 V}{\partial Q_i \partial Q_j}\Big|_{\mathbf{q},\mathbf{Q}=0}.
\end{aligned} \tag{13}$$

These couplings are used within FGR, see Eq. (7), to compute the phonon-induced transition rates between *system* vibrational eigenstates ϕ_i and ϕ_f. Thermal averaging over the initial states and summing over the final *bath* states allows one to account for the thermal population of the bath oscillators at finite temperature ($T \neq 0$ K) and the respective upward rates. Further details, such as the employed atomistic model, the utilized calculation methods, and a detailed analysis, can be found in Appendix C.

Based on the theoretical treatment outlined here we calculate all individual one- ($\Gamma^{(1)}$) and two-phonon transition ($\Gamma^{(2)}$) rates and ultimately the vibrational lifetime of the fundamental transition. For the first eigenstate, the lifetime is given by

$$\tau_1^{-1} = \left(\Gamma_{1,0}^{(1),\downarrow} + \Gamma_{1,0}^{(2),\downarrow}\right) - \left(\Gamma_{0,1}^{(1),\uparrow} + \Gamma_{0,1}^{(2),\uparrow}\right), \tag{14}$$

with the vibrational relaxation rates obeying the detailed balance condition. The final lifetime τ_1 together with its temperature dependence is shown in Fig. 6. The decreasing lifetime with increasing temperature is a consequence of temperature-dependent weight factors in the rate expressions based on Fermi's golden rule in addition to the temperature-dependent upwards rates $\Gamma_{0,1}^{\uparrow}$. Additional information and details can be found in Appendix C.

In practice, our model potential possesses 32 bound states below the barrier, see Fig. 5 and Table I, for

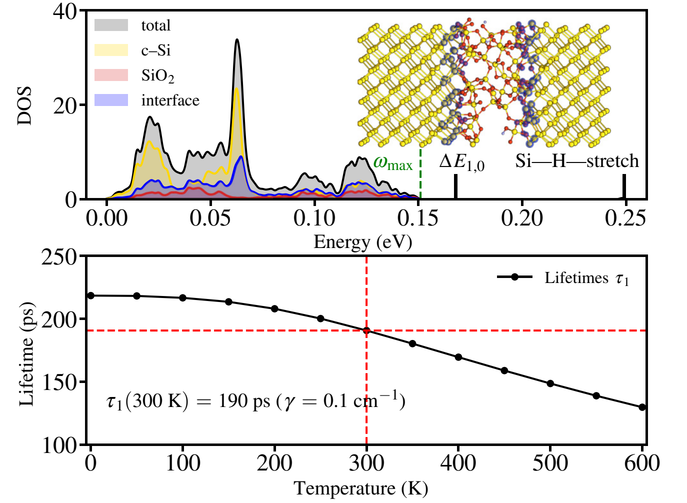

FIG. 6. Upper panel: phonon density of states together with the Si/SiO_2 interface model used for the calculations. The energy of the system mode is highlighted as $\Delta E_{1,0}$. Furthermore, the contributions of different regions to the total DOS are shown. Lower panel: the lifetime of the first vibrational eigenstate $|\phi_{1,L}\rangle$ over a wide range of temperatures. The parameter γ is the width of the Lorentzian broadening.

which we would need to calculate all individual relaxation rates $\Gamma_{i,f}$. For τ_2 this would mean computing $\Gamma_{2,1}$ and $\Gamma_{2,0}$ and the corresponding upward rates. However, $\Delta E_{2,0}$ is more than twice the largest phonon mode ω_{max} of the Si/SiO_2 system, see Table I and Fig. 6, which is beyond the two-phonon dissipations considered here. For all practical applications we therefore employ an idealized harmonic model [27,42,74,80], meaning that we split the model potential $V(q)$ into two harmonic oscillators. Within this simplified approach the selection rule $\Delta n = \pm 1$ applies and transitions between the oscillators are prohibited. The corresponding single-phonon scaling law for the vibrational lifetime of an eigenstate $|\phi_n\rangle$ is then given by

$$\tau_n = \frac{\tau_1}{n}, \tag{15}$$

with τ_1 being the lifetime of the first eigenstate as calculated above. A detailed discussion and motivation is given in Appendix C.

E. Dipole scattering

Next we turn to the rate expressions for inelastic induced excitations. Such excitation mechanisms are usually caused by *external* perturbations, e.g., applied electric fields or energetic charge carriers (e.g., in STM experiments or current flowing in a MOSFET). As already mentioned in Sec. II, one inelastic excitation channel is related to the electric field caused by electrons. This field can interact with the dipole created by the vibration of

the adsorbate and induce transitions between vibrational levels. These *dipole scattering* rates are due to an electrostatic coupling to the transition dipole moment μ and can be calculated by a formula derived by Persson *et al.* [60,81,82]

$$\Gamma_{i,f}^{\mathrm{dip}} = \frac{I}{e} \left| \frac{\langle \phi_f | \boldsymbol{\mu} | \phi_i \rangle}{e a_0} \right|^2, \tag{16}$$

where e is the elementary charge, a_0 the Bohr radius, $\hat{\mu}$ the dipole moment, and I the current. Quite contrary to STM experiments where the tunneling current is perpendicular to the surface, the current density in the channel of a MOSFET is parallel to the (100) surface. On the other hand, a typical STM tunneling current of 1 nA [23,41,58] can lead to a current density of 10^9 A/m^2, which is comparable to the operating current densities in modern transistors. In Appendix D we use the dissociation path shown in Fig. 5 and Ref. [26] and demonstrate that the interaction of the Si–H bond along the proposed trajectory with an electric field is indeed very weak.

F. Resonance scattering

As already mentioned in Sec. II another possible excitation channel is related to electronic resonances. A *resonance scattering* model accounts for electrons tunneling into unoccupied states of the adsorbate, the LUMO of the Si—H bond, forming a temporal negative ion state. Thereby the internuclear potential is changed, inducing a nuclear relaxation of the system. When the electron returns to the substrate, an inelastic relaxation process transfers energy to the *system*, leaving the neutral ground-state PEC in a vibrational excited state. The same mechanism applies to a hole scattering into an occupied orbital of the Si—H complex and forming a cationic resonance. Two formulations of a vibrational heating model for this mechanism have been developed by Persson *et al.* [83] and Salam *et al.* [84]: an *incoherent* multiple single-step process [85] and a theory of *coherent* multiple vibrational excitations [84]. Both variants are schematically illustrated in Fig. 7. Whereas the *incoherent* model requires a rather high current (scattering electrons and holes) compared to the vibrational lifetime, the *coherent* formulation allows overtone transitions, which results in an excitation path with a smaller number of intermediate steps on the bond-breakage ladder [86,87]. Recent experimental results [57] have shown that indeed less electrons are needed to dissociate H than expected from the *incoherent* formulation and, hence, support the proposed *coherent* formulation. We utilize the expression for the transition rate based on the formulation in Ref. [88]. In this formulation it is assumed that an electron with incident energy ϵ can induce an excitation from state $|\phi_i\rangle$ to $|\phi_f\rangle$ via the vibrational eigenstate

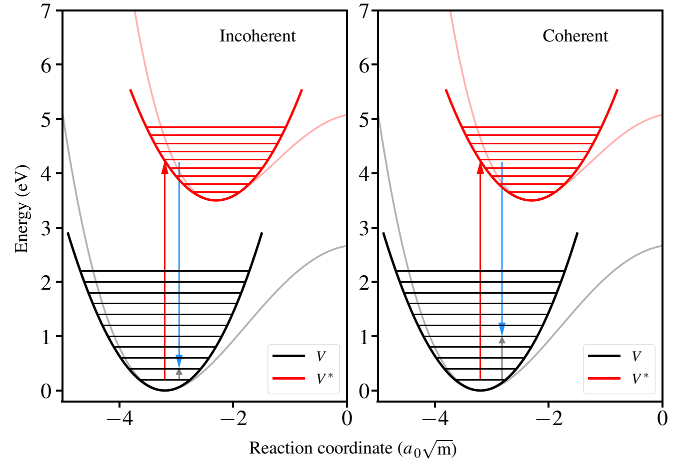

FIG. 7. Schematics showing the two different vibrational heating models describing the resonant scattering interaction of tunneling carriers. In a first step, the electron creates a negatively charged complex by temporarily occupying a resonance state, denoted by V^* (or a cationic system induced by a hole resonance). Left: incoherent multiple single-step process. Each electron is only able to transfer one quantum of energy during the inelastic relaxation process. As a consequence such a subsequent ladder-climbing mechanism requires as many electrons as eigenstates of the bond. Right: the coherent multiple vibrational excitation formulation allows for overtone transitions and hence a shorter excitation path.

$|\psi_j\rangle$ of the resonance with

$$\Gamma_{i,f}^{\mathrm{res}} = \frac{4\Delta_{\mathrm{res}}^2}{\pi\hbar} \int d\epsilon f(T,\epsilon)\,[1 - f(T,\epsilon)] \times \left| \sum_j \frac{\langle \phi_f | \psi_j \rangle \langle \psi_j | \phi_i \rangle}{\epsilon_{\mathrm{res}} - \epsilon + \epsilon_i - \epsilon_j + i\Delta_{\mathrm{res}}} \right|^2. \tag{17}$$

This expression includes the energetic position of the resonance with respect to the Fermi level, ϵ_{res}, its width as the inverse of the resonance lifetime, $\Delta_{\mathrm{res}} = \hbar/\tau_{\mathrm{res}}$, as well as the energies of the eigenstates $|\phi_i\rangle$ and $|\psi_j\rangle$. Furthermore, it accounts for the energy distribution function $f(\epsilon)$ of charge carriers at the interface calculated from the Boltzmann transport equation, see Eqs. (1) and (3), which is a crucial ingredient as pointed out in Sec. I, and generally depends on the position within the MOSFET. Hence, inelastic resonance scattering rates do depend on the spatial position along the channel–oxide interface. All parameters but one can be extracted (or approximated) from DFT results, see Appendix B, e.g. the PECs and wave functions for the charged Si—H-complex as well as the position of the resonances. For the resonance width Δ_{res}, however, we have to rely on literature values [38,39,80,89].

G. Macroscopic properties

Based on the theoretical treatment introduced above, we propose a model for describing hot-carrier-induced damage at the Si/SiO_2 interface. Our approach, as summarized in Fig. 2, includes all the aforementioned processes, namely the vibrational relaxation mechanism, Eq. (15), as well as the inelastic channels, dipole, Eq. (16), and resonance scattering, Eq. (17). As discussed above, the coherent formulation of the inelastic resonance scattering mechanism, see Fig. 7, naturally maps the SP and MP process discussed in the Introduction onto a single physical mechanism. This particular formulation accounts for neighboring transitions (ladder climbing, MP) as well as transitions to higher excited states (overtone transitions, SP). We recall that although such a resonance-based excitation mechanism was already proposed by the group of Hess, see Ref. [23], it has not been rigorously included in any calculations so far. Finally, combining all these mechanisms, the total Si–H excitation rate from its vibrational eigenstate $|\phi_i\rangle$ to $|\phi_f\rangle$ is given by Eq. (8).

Eventually breaking of the Si–H bond and creating an electrically active interface defect is associated with the transition from the *left* to the *right* well of the ground-state PEC. The bond-breaking rate Γ^{break} can be defined through time propagation of the density matrix ρ_S where the dynamics of the individual populations P_i of each left—or right—localized eigenstate $\phi_{i,L/R}$ need to be calculated. Hence, the equations of motion for the density matrix

$$\frac{\partial \rho_{S,i}}{\partial t} = \sum_{j\neq i} \left[\Gamma_{j,i}\rho_{S,j}(t) - \Gamma_{i,j}\rho_{S,i}(t)\right], \tag{18}$$

are solved using the method of matrix exponentials for a total propagation time up to 1 μs. Due to the density matrix being set up in the basis of the localized vibrational eigenstates of the ground-state PEC $V(q)$, the diagonal elements can be interpreted as the respective populations $P_i(t)$.

Starting with a full localization in the *left* well of $V(q)$, e.g., $P_0(t=0)=1, P_{i\neq 0}=0$, the transition, or bond-breakage rate Γ^{break} can be defined as

$$\Gamma^{\text{break}} = -\frac{dP_L(t)}{dt} = \frac{dP_R(t)}{dt}, \tag{19}$$

assuming a negligible back flow of population. $P_{L,R}(t)$ are the total populations of the left and right well, respectively, at time t.

Knowing the bond-breaking rate Γ^{break} allows us to formulate a reaction equation for the evolution of the concentration of broken and intact Si—H bonds with stress time. For the forward reaction we assume, as in Refs. [5,90,91], two possible states, an intact Si—H bond (left well), and a broken state (right well) describing a P_b center and the released H atom. Experimental evidence clearly suggests that the backward reaction, passivating the P_b center with one hydrogen, proceeds via a different reaction [91–93], namely by breaking of a H_2 molecule. Once the hydrogen is in the next but one bond-center site, it is likely that the resulting P_b center becomes charged [14,31,94,95]. Similarly, due to its *negative-U* character [96–98], the hydrogen will become charged as well. As was shown in the work of Pantelides *et al.* [99–101], charged hydrogen species face a rather small migration barrier for moving laterally within the subinterfacial Si region (0.3–0.5 eV), while the potential barrier to cross over into the SiO_2 side is at least twice as large. Thus, once the H is released and potentially charged, it would be mobile along the interface and thereby potentially able to trigger additional reactions, e.g., the formation of H_2, which has almost no formation barrier.

The reaction equation including the aforementioned chemical reactions is

$$\frac{d\,[\text{SiH}]}{dt} = -\Gamma^{\text{break}}\,[\text{SiH}] + \Gamma^{\text{pass}}\,[\text{H}_2]\,[P_b], \tag{20}$$

where Γ^{pass} describes cracking of H_2 and the subsequent passivation of P_b via $Si_3 \equiv Si^{\bullet} + H_2 \rightarrow Si_3 \equiv SiH + H$. According to Refs. [90,93,102] this process is purely thermally activated and the rate constant is given by an Arrhenius equation $\Gamma^{\text{pass}} = \Gamma_0^{\text{pass}}\exp(-E_{\text{pass}}/k_BT)$ superimposed with a Gaussian distribution of the passivation energy E_{pass}. The inferred parameters are $\langle E_p\rangle \sim 1.51$ eV, $\sigma_{E_p} \sim 0.12$ eV, and $\Gamma_0^{\text{pass}} = 1.43\times 10^{12}$ $\text{cm}^3\ \text{s}^{-1}$, which were also used in a recent study to model the recovery of HCD-induced damage in an actual MOSFET [92,103].

In addition, one equation describing the conservation of pristine Si—H bonds is introduced as

$$[\text{SiH}] + [P_b] = [\text{SiH}]_{\text{tot}}, \tag{21}$$

while the value for $[H_2]$ is set to a constant concentration of 5×10^{17} cm^{-3}, given by the physical solubility of H_2 in vitreous silica [104]. Introducing the quantity $N_0 \mathrel{\widehat{=}} [\text{SiH}]_{\text{tot}}$ and solving for $f_{\text{Pb}} \mathrel{\widehat{=}} [P_b]/N_0 = 1 - [\text{SiH}]/N_0$, the probability that a bond is broken, is then given by

$$\frac{\partial f_{\text{Pb}}}{\partial t} = (1 - f_{\text{Pb}})\,\Gamma^{\text{break}} - f_{\text{Pb}}\widetilde{\Gamma}^{\text{pass}}, \tag{22}$$

where $\widetilde{\Gamma}^{\text{pass}} = \Gamma^{\text{pass}}[H_2]$.

The interfacial defect density $N_{\text{it}}(x, t_{\text{stress}})$, i.e., the number of created P_b centers, is calculated along the silicon-oxide interface for each stress time t_{stress}. Due to the P_b center being an active defect with levels in the silicon band gap, upon charge capture it perturbs the device electrostatics and degrades the mobility of charge carriers inside the channel. Hence, the calculated $N_{\text{it}}(x, t_{\text{stress}})$ profile determines the degradation characteristics of the MOSFET, such as the change of its linear drain current over time, $\Delta I_{D,\text{lin}}$.

IV. RESULTS

With the parameters extracted from *ab inito* DFT calculations (see Appendix B), we are able to apply our developed model to describe the effects of hot carriers in electronic devices.

Two different devices and several stress conditions have been chosen for the modeling benchmark. A pMOSFET with a gate length of 100 nm and an nMOSFET with a gate length of 65 nm. Both technologies employ 2.2-nm SiON as the gate oxide and have an operating voltage of $|V_{\rm DD}| = 1.5$ V. The devices are stressed at room temperature, $T = 298$ K and are subjected to their respective worst-case stress conditions, namely $V_G = -1.5$ V and $V_D = -1.8$, -2.3 and -2.8 V for the pMOS and $V_G = V_D = 1.8$, 2.0 and 2.2 V for the nMOS device. To monitor the degradation characteristics, $\Delta I_{D,\rm lin}$ traces up to 10 ks of stress are recorded.

Due to the applied stress bias resulting in a nonequilibrium carrier ensemble along the channel-oxide interface, the carrier energy distribution function yields useful information on the state of the charge carriers in the semiconductor device. Hence, our framework couples our theoretical modeling approach to a solution of the Boltzmann transport equation, see Sec. III. Interface state profiles $N_{\rm it}(x, t_{\rm stress})$ along the Si/SiON interface have been calculated using the formalism described above and subsequently the degradation trend has been calculated using modern TCAD tools [71,72]. As a measure of hot-carrier damage we experimentally extract the change of the linear drain current of the devices, denoted as $\Delta I_{d,\rm lin}(t)$ traces. The final results comparing the simulations of our framework with the respective experimental data are shown in Fig. 8 and show a very good agreement with the experimental data allowing for a reasonable optimization of the extracted parameters.

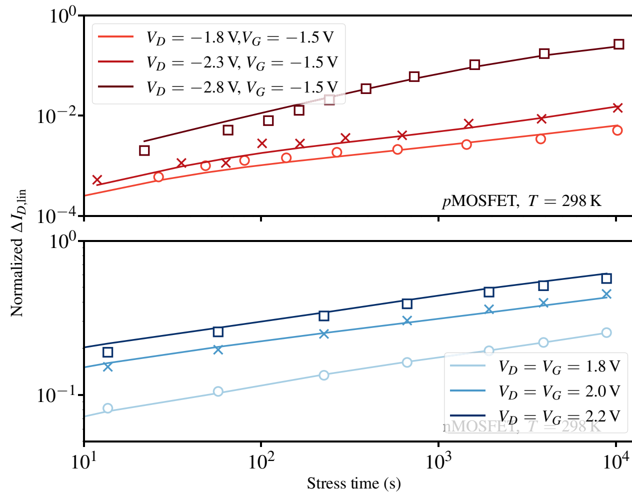

FIG. 8. Measurement (symbols) and simulations (lines) for the model benchmark. The simulation framework is validated against experimental data of a 65-nm nMOSFET and a 100-nm pMOSFET subjected to three different hot-carrier stress conditions each. The model shows very good agreement with the measured characteristics for all bias conditions.

V. DISCUSSION

We highlight some findings and features of our model. Throughout this work a unique, albeit slightly optimized parameter set is used to describe the effects of hot-carrier degradation in both devices, see Fig. 9 and the table therein. All parameters are within a reasonable range and close to reported values in the literature and our own DFT results (see Appendix B). Only two parameters are

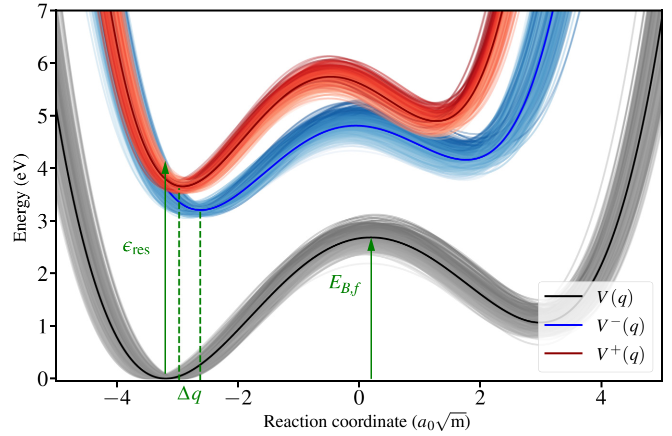

Parameter	Units	Model	DFT Results	Refs.
$E_{B,f}$	(eV)	2.7	2.57 [26]	2.83[91, 103]
$\sigma_{E_{B,f}}$	(eV)	0.12	0.20 [26]	0.08[91, 103]
$\epsilon_{{\rm res},n}$	(eV)	3.24	3.65	2.7 [39]–4.10 [81, 90]
$\sigma_{\epsilon_{{\rm res},n}}$	(eV)	0.21	–	–
$\Delta_{{\rm res},n}$	(eV)	0.17	–	1.0 [39]–1.6 [81, 90]
Δq_n	$(a_0\sqrt{\rm m})$	0.58	0.9	–
$\sigma_{\Delta q_n}$	$(a_0\sqrt{\rm m})$	0.085	–	–
$\epsilon_{{\rm res},p}$	(eV)	3.74	3.96	4.80 [38]
$\sigma_{\epsilon_{{\rm res},p}}$	(eV)	0.29	–	–
$\Delta_{{\rm res},p}$	(eV)	0.12	–	0.6 [39]
Δq_p	$(a_0\sqrt{\rm m})$	0.23	0.45	–
$\sigma_{\Delta q_p}$	$(a_0\sqrt{\rm m})$	0.09	–	–
τ_1	(ns)	0.39	0.19	$1-1.5$ [75, 76, 78, 80]

FIG. 9. The different PECs together with the parameters for the negative (subscript n) and positive (subscript p) ion resonance, see Sec. III, used to represent the experimental data. Due to the amorphous nature of the Si/SiO_2 interface, quantities such as the barriers are assumed to be normally distributed. Additionally, a comparison to our own results obtained from DFT simulations as well as literature values is given.

associated with a higher degree of uncertainty for which we have to rely solely on our own calculations or literature values. The first uncertain parameter is the resonance width $\Delta\epsilon_{\mathrm{res}}$, which was calculated by Stokbro *et al.* [39,39] to be 1 eV for the anionic and 0.6 eV for the cationic resonance state, respectively. However, for a typical resonance lifetime [80,89,105] of $\tau_{\mathrm{res}} = \hbar/\Delta_{\mathrm{res}} \sim 1 - 2$ fs, the width is about $0.3 - 0.7$ eV. The second difficult to ascertain parameter is the shift of the equilibrium position of the excited potential energy curves with respect to the ground-state minimum. Our own calculations, see Appendix B, suggest a shift of approximately 0.4 $\mathrm{a}_0\sqrt{\mathrm{m}}$ for the positively charged PEC and approximately 0.9 $\mathrm{a}_0\sqrt{\mathrm{m}}$ for the negative PEC, which served as an input for our model. Note that, due to the amorphous interface, an intrinsic distribution of these quantities is, however, to be expected. Thus, in total 750 unique configurations with individual PECs and resonances are used by randomly selecting normally distributed parameters, see Fig. 9, where the resulting quantities are listed in the table.

Finally, to give insights into the degradation processes, Fig. 10 shows the rate matrix of one Si—H bond potential with 20 eigenstates localized in the left well together with the EDFs and the time-dependent populations of the density matrix. Three selected spatial positions along the channel-oxide interface, from source to drain, for both

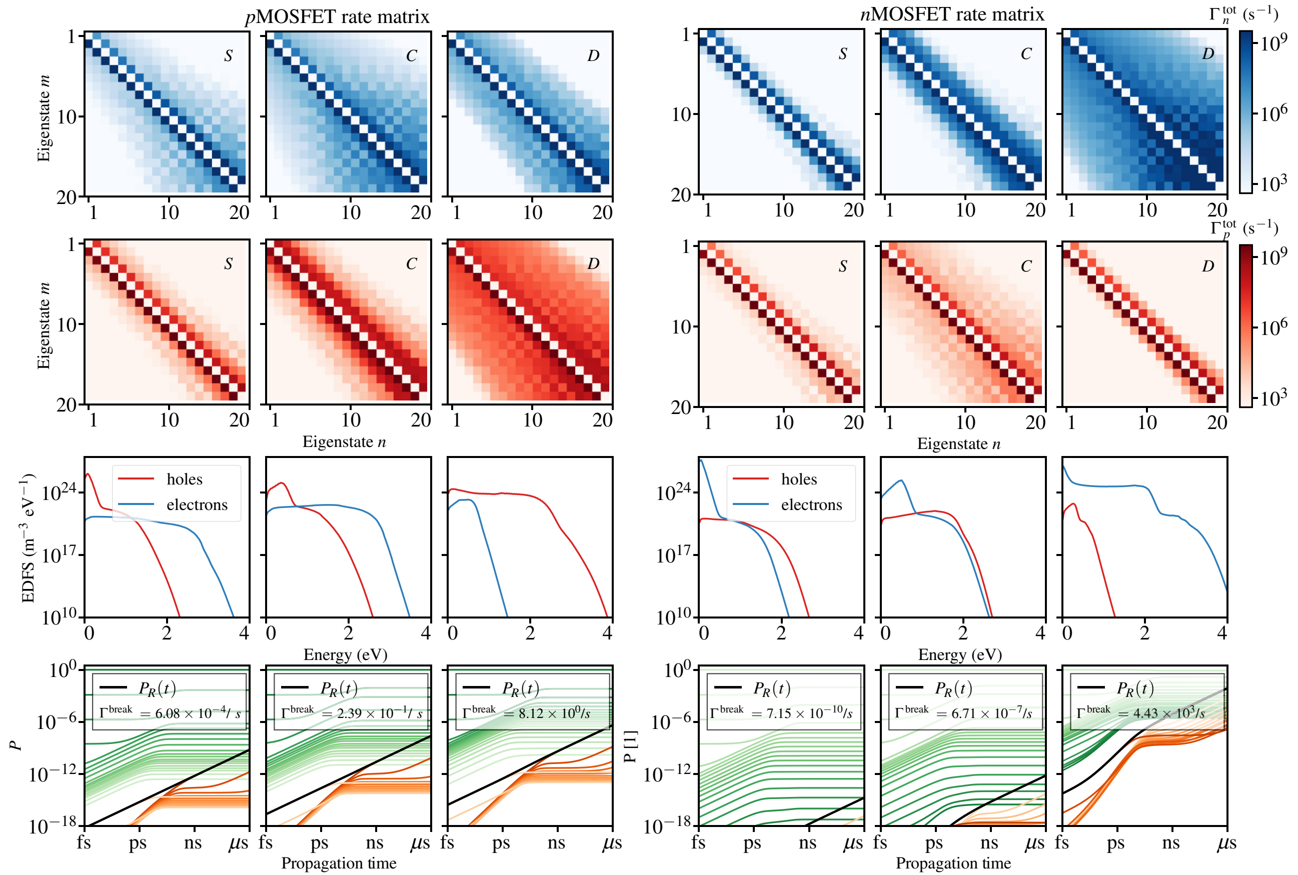

FIG. 10. The density matrix projected onto the *left* well of a full model potential containing 20 eigenstates ϕ_L evaluated at three different positions along the silicon-oxide interface, namely the source side (S) of the devices, the channel region (C) and the drain (D) end. Both, the pMOSFET (left) and nMOSFET (right) are shown in the graph. The total matrix is split into contributions from electrons (Γ_n^{tot}) and holes (Γ_p^{tot}) for a better representation of their respective contribution. Clearly visible are the small upward rates due to minority carriers at the source side and in the channel region. On the other hand, the accumulation of energetic carriers at the drain end results in the formation of a temporary excited state due to the resonance-mediated excitation process. Secondary generated carriers, which have been accelerated towards the source side, compare the EDFs in the third line, seem to dominate the Si—H dynamics in the respective regions in the pMOS, whereas the contributions of holes in the nMOS device is rather negligible. The lower panels show the time propagation of the *full* density matrix (green, left-well localized eigenstates; orange, right-well localized eigenstates, from dark to light: $\phi_{L/R,0}..\phi_{L/R,i}$), which, due to the eigenstate representation can be considered as the populations. The bond-breakage rates are calculated as the change of the populations with time, $\Gamma^{\mathrm{break}} = dP_R(t)/dt$, assuming a negligible back flow. One can clearly see that electrons are more efficient in triggering excitations of the vibrational eigenstates of the Si—H bond and hence result in an enhancement of the dissociation rate.

MOSFETs are shown in Fig. 10. Minority carriers—holes in the pFET and electrons in the nFET—at the source side of the device are close to equilibrium, see the EDFs in Fig. 10, and thus are not able to scatter into either electronic resonance. Hence, the upper triangle of the rate matrix, which represents excitation, is mainly determined by dipole-induced upward rates and the detailed balance condition at the given temperature. However, along the channel carriers are accelerated by the electric field and exchange energy via various scattering mechanisms, resulting in a substantial fraction of *hot* carriers at the drain side. These carriers have a strongly nonequilibrium EDF as seen from the solution of the Boltzmann transport equation. Such a high energy tail enables the formation and transient occupation of an ionic resonance, allowing for excitations to higher-lying eigenstates visible as large off-diagonal elements in the rate matrices, see Fig. 10. Additionally, the effect of impact ionization aids the excitation and dissociation of Si—H bonds at the interface via energetic secondary generated carriers, see Fig. 10, which shows the electron rate matrices for the pMOS and the excitation rates Γ_p^{tot} induced by holes in the nMOS device. Whereas for the nMOS this component is rather weak and negligible, see the right panels of Fig. 10, secondary generated electrons in the pMOS account for a major contribution to the overall excitation rates. Particularly in the channel region and towards the source side, electrons with sufficient energy to scatter into the available anionic resonance state are present, see the left panels of Fig. 10.

The disparity between electrons and holes is a direct consequence of a key ingredient in the modeling framework introduced in Sec. III, namely the impact of different electronic resonance states accessible for electrons and holes. The available electronic scattering state for electrons is approximately 0.4 eV lower in energy compared to the hole resonance. Furthermore, the minimum of the PEC for the excited anionic complex is shifted twice as much with respect to the ground-state minimum compared to the cationic equilibrium position. This enhances the probability of overtone transitions due to the overlap integral of the wave functions included within the resonance-mediated formulation, see Eq. (17) in Sec. III. Hence, electrons, despite having a similar EDF, are more efficient in exciting and breaking Si—H bonds. This is particularly visible at the drain end of both devices. Although the EDFs for electrons and holes are comparable within this region, see the respective panels in Fig. 10, the rates calculated from the time propagation of the density matrix, see the lower panels in Fig. 10 [blue lines are the populations of the vibrational eigenstates in the left well ϕ_L, purple lines represent the right-well populations, and the black line shows $P_R(t)$], differ by 2 to 3 orders of magnitude. Additionally, secondary generated holes in the channel region of the nMOS do not contribute at all to the creation of damage, while electrons generated by impact ionization in the pMOS clearly dominate the degradation in this region.

VI. CONCLUSIONS

Advances in processing and fabrication have enabled the relentless downscaling into the nanometer regime and have opened the way for alternative device structures and materials. Approaching the atomic scale, understanding individual defect properties and their interaction with the surrounding start to become a decisive factor for device reliability and device performance. Keeping pace with the technological progress on the theoretical simulation side, hence, requires an in-depth description of the reliability phenomena including the involved mechanisms.

In this work, we develop a fundamental understanding of a particularly detrimental reliability issue in modern semiconductor technology known as hot-carrier degradation [20,21,23]. HCD is known to create defects at the channel-oxide interface triggered by the interaction of energetic (hot) carriers with Si—H bonds and their subsequent breakage. We identify a resonance-based excitation mechanism being responsible for this interaction, where a temporarily charged Si—H complex is formed and upon inelastic electronic relaxation induces multiple vibrational excitations in its ground state. Such a process has also been found and described in previous studies using dedicated experiments such as scanning tunneling microscopy [40,43,44,46,53,57]. Its strong current dependence together with the moderate carrier energies needed to trigger this excitation channel agree well with the characteristics of HCD. Our quantum kinetic approach is based on the open-system density-matrix theory to describe hot-carrier-induced interactions and damage in electronic devices. Useful system-bath interactions such as vibrational relaxation, dipole scattering as well as resonance scattering, are included in our model formulation. The essential parameters entering the calculations of the individual rates can be extracted (or approximated) from *ab initio* studies. Combined with a thorough transport simulation, the presented approach allows an accurate microscopic description of HCD at the device level and the performed simulations are in very good agreement with experimental trends.

Besides the physical meaningful interpretation our results provide, we want to highlight another finding, which is a direct consequence of our approach: our derived formulation allows for an intuitive understanding of a peculiarity of HCD. Occasional reports show that the degradation caused by HCD in nMOS devices is larger than that of their pMOS counterparts [9,106–108]. Taking into account that the available resonance states for holes is higher in energy than for electrons, as suggested by our own DFT results and previous literature studies [23,38,39], it is less likely for holes to trigger bond

excitation and dissociation, which provides a physically reasonable explanation of this observation.

Finally, we would like to mention that the complete framework derived and described within this work is free of empirical or phenomenological parameters. Thus, it can easily be generalized to describe the interactions of emerging material combinations, e.g., HCD-related issues in Si-Ge–based devices [109] or the interaction of hydrogen graphene [110], and hence is applicable also for future technologies.

ACKNOWLEDGMENTS

The work is supported in part by the Austrian Research Promotion Agency (FFG, Take–Off Program) under Project No. 861022, in part by Austrian Science Fund (FWF) under Grant No. P31204-N30, and in part by the European Union's Horizon 2020 Research and Innovation Programme under the Marie Sklodowska-Curie Grant Agreement No. 794950. Furthermore, the authors acknowledge financial support from the Deutsche Forschungsgemeinschaft (DFG) through Projects No. BO 4623/1-2 and No. SA 547/9-2 as well as support by the Vienna Scientific Cluster for providing resources on the Austrian high-performance cluster VSC4.

APPENDIX A

In the following we discuss additional simulation results such as the formation of an anionic or a cationic system as well the interaction of an electric field with the Si—H dipole moment vector along the reaction coordinate. Furthermore, we explicitly calculate the vibrational decay rates for the Si—H system based on a perturbation theory approach according to Fermi's golden rule. For our calculations we use a combination of classical interatomic potentials and DFT applied on the Si—H bond within a realistic Si/SiO_2 environment. The DFT calculations are carried out within the CP2K package [111], which uses a mixed Gaussian and plane-wave approach to represents the electrons within the three-dimensional periodic Si/SiO_2 system. The PBE functional in conjunction with a double-ζ Gaussian basis set and the Goedecker-Teter-Hutter (GTH) pseudopotentials is used, with the plane-wave cutoff set to 1200 Ry. Additionally, calculations employing the classical ReaxFF force field [78] are conducted using the molecular dynamics engine LAMMPS [112]. Further information and technical details are discussed in our recent work, see Ref. [26].

APPENDIX B: POTENTIAL ENERGY CURVES AND RESONANCES

A major ingredient of the proposed model is the potential energy curve along the reaction coordinate of the Si—H dissociation process. In surface science individual dynamics like H dissociation or switching on Si surfaces can be selectively monitored by carefully tuning the STM parameters and sample preparation [38,43,89,105]. Conversely, understanding the trajectory of Si—H bond breakage at an Si/SiO_2 interface is more complex and still an active research topic. In a recent theoretical study [26], we propose a mechanism where in an initial step the hydrogen bends towards an adjacent silicon atom, and subsequently moves into a bond-center site on the Si side of the interface between the next-nearest Si—Si bond. The *ab initio*-derived potential energy curve together with the model potential along the mass-weighted reaction coordinate, which is a combination of the Si—H bending and stretching mode, is shown in Fig. 11.

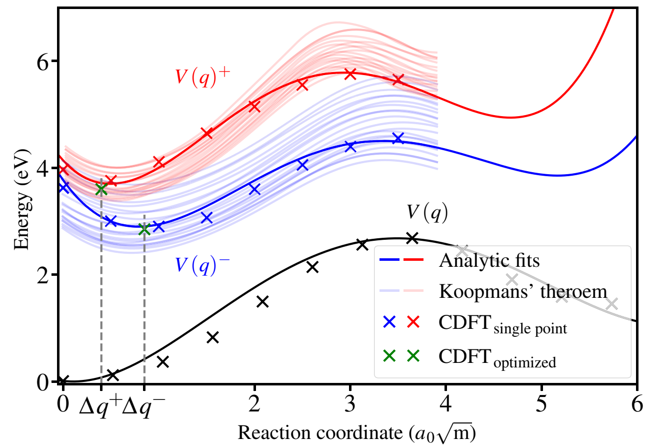

FIG. 11. Potential energy curves along the reaction coordinate, see Ref. [26]. Two approximations are used to construct the resonance profiles for the excited complexes V^*: Koopmans' theorem using the energies of the ten lowest unoccupied α- and β-spin orbitals, and the method of constrained density-functional theory to directly assess the respective diabatic states.

Furthermore, the theoretical treatment of resonance-induced excitations requires the knowledge of the involved excited state. An electron (or hole) scattering into a resonance forms a temporary anionic (cationic) system, which evolves within its lifetime on the excited potential V*. Thus, three parameters need to be known which enter the calculation of $\Gamma_{i,f}^{\mathrm{res}}$ in Eq. (17): the energetic position of the resonance ϵ_{res}, its lifetime τ_{res} and the excited potential energy curve V^* along the reaction coordinate. Unfortunately, excited-state properties and dynamics are very difficult to calculate and hardly accessible within standard density-functional theory. A popular method of approximating excited anion or cation potential energy curves is to apply Koopmans' theorem [80,113]. Within Koopmans' theorem the negative of the energies of the HOMOs and LUMOs can be related to the ionization potentials and electron affinities, respectively. Therefore, the orbital energies $E_{\mathrm{HOMO-LUMO}}$ can be used to approximate the resonance energy and the exited PECs. The cluster model

used within this calculation consists of 10 Si atoms and 22 H atoms, needed to passivate the Si atoms, additionally to the H representing the Si—H bond. 150 single-point calculations along the reaction coordinate, calculated in Ref. [26], are carried out. The resulting ten lowest unoccupied α and β-spin states are used to construct adiabatic resonance PECs, see Fig. 11.

The approximated energies of the corresponding resonance states at $q = 0$ is between 2.7 and 4.2 eV for the anionic states, whereas the cationic state is approximately 0.5 eV higher in energy. These results are in a reasonable agreement with previous findings [38,39,43,89,105]. All resonance profiles, for the negatively and positively charged state, have in common that their transition barrier is lowered compared to the ground-state potential as well as a shifted minimum configuration for the left well with respect to the neutral PEC. While the anionic PECs $V^{-}(q)$ possess barriers of approximately $1.4 - 1.7$ eV together with a shifted minimum of the left well by $\Delta q = 0.74 - 0.96\ \mathrm{a_0}\sqrt{\mathrm{m}}$ towards the transition barrier, the cationic resonances $V^{+}(q)$ are only shifted by around $\Delta q = 0.45\ \mathrm{a_0}\sqrt{\mathrm{m}}$ with an activation energy of approximately 2.0 eV. However, these calculations provide only a qualitative understanding of the excited resonance curve.

In order to directly construct the diabatic potential energy curves we use the method of constrained density-functional theory) [114,115] as implemented in the CP2K package [111,116,117]. Within the CDFT calculations we use a Si/SiO_2 interface model containing 472 atoms and restrict the *additional* charge (negative and positive) including the α-spin channel to be localized on the Si—H bond, see Fig. 12. First, single-point CDFT calculations with fixed atomic positions along the *neutral* bond-breaking trajectory are performed. The effect of lattice relaxations is explicitly neglected due to the short resonance lifetime [39,105], which is on the order of a few femtoseconds. These calculations are restricted up to the transitions' state, where the Si—H bond can be considered to be broken, to ensure that the charge can actually be localized on the Si—H complex.

The results for both charge states are shown in Fig. 11 (symbols). The *diabatic* PECs agree well with the results obtained using Koopmans' theorem and again show a shifted minimum configuration for the anionic and cationic resonance as well as reduced transition barriers. At the equilibrium position of the neutral state the charge-localized states are 3.64 (negative) and 3.96 eV (positive) higher in energy. Similar results have been obtained in previous studies [38,39,43,89,105].

In order to understand the constructed charge-localized states, Fig. 12 shows the spin density of the α channel (spin up, red) and β channel (spin down, blue) for the negatively (left) and positively (right) charged configuration at the equilibrium position of the neutral state (at $q = 0\ \mathrm{a_0}\sqrt{\mathrm{m}}$). One can see that one unpaired electron (spin up) is indeed localized on the Si—H complex. Further investigations using the method of Bader charge analysis show a difference between the neutral and the charged complex of $\Delta(Q_{\mathrm{SiH}} - Q_{\mathrm{SiH^-}}) = -0.93$ e for the negative complex, and $\Delta(Q_{\mathrm{SiH}} - Q_{\mathrm{SiH^+}}) = 0.86$ e for the positive system, respectively. However, the electronic structure in the direct vicinity adjusts differently to the negative and positive charge state of the Si—H bond, see Fig. 12. Whereas the spin density, and hence the charge distribution, is rather asymmetric on the adjacent Si—Si bonds for the negative charge state, the restructuring of the charge is much more symmetric in the positively charged configuration. This suggests that structural reconfigurations of the system due to the introduced charge are more pronounced in the negative charge state compared to the positively charged Si—H complex.

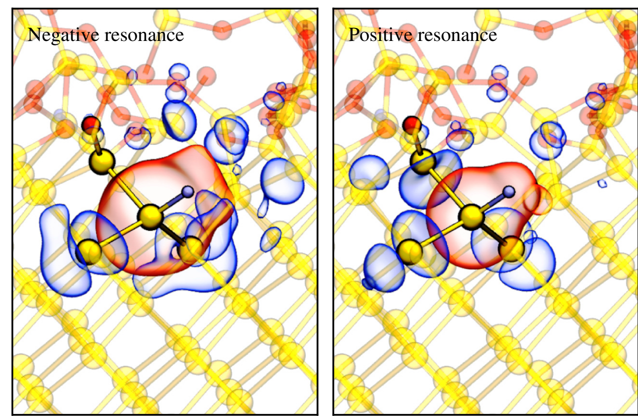

FIG. 12. The spin densities for the α– (spin up, red) and the β–channel (spin down, blue) of the negatively (left) and positively (right) charged Si—H complex. Clearly visible is that one unpaired electron in the α–channel is localized on the central Si—H bond. However, the electronic structure in the direct vicinity adjusts differently for both charge states, which indicates new structural equilibrium configurations for the charged system.

A more complete picture is provided by Fig. 13, which shows the results of full geometry optimizations within our CDFT simulation setup for both charge states. As to be expected, for the negatively charged Si—H complex the bonding distance changes from 1.48 Å to 1.75 Å and the Si—Si—H angle opens from approximately 109° to 141°. Such a structural reconfiguration forces the H atom towards the dissociation path and the transition barrier, see Figs. 13 and 11. The positive charge state, on the other hand, does not undergo such pronounced relaxation effects. The reconfigurations are mainly determined by the Si atom slightly moving out of its plane and thereby stretching the nearby Si—Si bonds and also the Si—H bond itself, see Fig. 13. This, however, potentially suggests a different bond-breakage trajectory in the positive charge state.

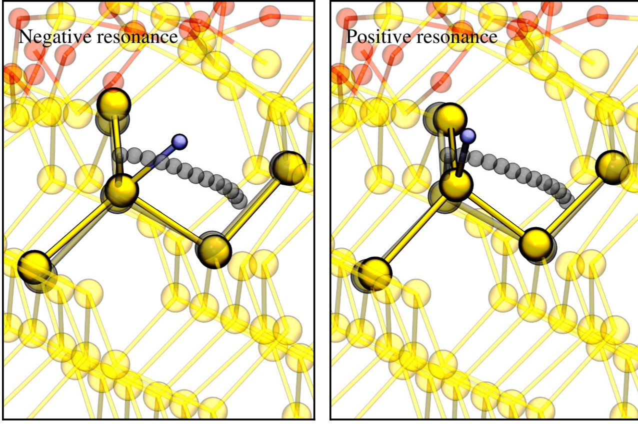

FIG. 13. Effects of structural relaxations for the charged Si—H complex including the bond–breaking trajectory for the neutral charge state, indicated as gray, transparent atoms, for a better comparison. For the negative charge state (left) the Si—H distance as well as the Si—Si—H angle increase, forcing the hydrogen in the direction of the (neutral) bond-breaking trajectory [26]. The positively charged configuration (right) does not show pronounced reconfigurations where only the central Si atom moves, which alters the bond lengths in the direct vicinity.

APPENDIX C: VIBRATIONAL LIFETIMES

Expanding on the results in Sec. III, here we show calculation details and give a systematic analysis by comparing our approach to well-known values in the literature. Following Refs. [74,77,118] and in particular Ref. [79], the *one-phonon* coupling term in Eqs. (12) and (13) yields the following rate expressions:

$$\Gamma_{i,f}^{(1),\downarrow} = \pi \sum_k |\langle\phi_i|\lambda_k(\mathbf{q})|\phi_f\rangle|^2 \frac{\langle n_k\rangle + 1}{\omega_k}\delta(\varepsilon_i - \varepsilon_f - \hbar\omega_k),$$
$$\Gamma_{i,f}^{(1),\uparrow} = \pi \sum_k |\langle\phi_i|\lambda_k(\mathbf{q})|\phi_f\rangle|^2 \frac{\langle n_k\rangle}{\omega_k}\delta(\varepsilon_i - \varepsilon_f + \hbar\omega_k), \tag{C1}$$

where $\langle n_k\rangle = \sum_n n p_{n,k}(T)$ is the thermally averaged quantum number of the kth bath mode with $p_{n,k}(T)$ being the thermal population of its nth level. However, if $\Delta E_{1,0}$ is greater than $\omega_{\max}$, the highest phonon frequency, *two-phonon* terms become relevant. The corresponding rates for the simultaneous (de)excitation of two different bath modes are given by

$$\Gamma_{i,f}^{(2a),\downarrow} = \frac{\pi\hbar}{8} \sum_{k\neq l} |\langle\phi_i|\Lambda_{k,l}(\mathbf{q})|\phi_f\rangle|^2 \frac{\langle n_k\rangle + 1}{\omega_k}\frac{\langle n_l\rangle + 1}{\omega_l}$$
$$\delta(\varepsilon_i - \varepsilon_f - \hbar\omega_k - \hbar\omega_l),$$
$$\Gamma_{i,f}^{(2a),\uparrow} = \frac{\pi\hbar}{8} \sum_{k\neq l} |\langle\phi_i|\Lambda_{k,l}(\mathbf{q})|\phi_f\rangle|^2 \frac{\langle n_k\rangle}{\omega_k}\frac{\langle n_l\rangle}{\omega_l}$$
$$\delta(\varepsilon_i - \varepsilon_f + \hbar\omega_k + \hbar\omega_l), \tag{C2}$$

whereas the expression for two identical bath modes is

$$\Gamma_{i,f}^{(2b),\downarrow} = \frac{\pi\hbar}{8} \sum_{k} |\langle\phi_i|\Lambda_{k,k}(\mathbf{q})|\phi_f\rangle|^2 \frac{\langle n_k^2\rangle + 3\langle n_k^2\rangle + 2}{\omega_k^2}$$
$$\delta(\varepsilon_i - \varepsilon_f - 2\hbar\omega_k),$$
$$\Gamma_{i,f}^{(2b),\uparrow} = \frac{\pi\hbar}{8} \sum_{k} |\langle\phi_i|\Lambda_{k,k}(\mathbf{q})|\phi_f\rangle|^2 \frac{\langle n_k^2\rangle - \langle n_k^2\rangle}{\omega_k^2}$$
$$\delta(\varepsilon_i - \varepsilon_f + 2\hbar\omega_k). \tag{C3}$$

For the sake of completeness it should be mentioned that two-phonon processes also give rise to the simultaneous creation and annihilation of phonons, however, this contribution can be neglected. For all practical applications, the δ functions in Eqs. (C1)–(C3) need to be replaced by functions with a finite broadening, e.g., Lorentzians

$$\delta(E) \rightarrow \frac{1}{\pi}\frac{\gamma}{\gamma^2 + E^2}, \tag{C4}$$

with the broadening parameter γ.

The systems studied here are (a) a H-passivated Si(100) surface (500-atom model) and, on the other hand, (b) a Si(100)/amorphous SiO_2 interface system (472-atom model). Both systems are investigated using DFT to identify the system mode of interest. For (a) we perform a normal-mode analysis and select one of the 24 normal modes, which could be classified as Si—H bending modes, see Fig. 14. We choose a Si—H bending mode due to its comparability to recent theoretical studies [74,77,79] and in order to ultimately benchmark our approach. Frequencies up to around $\omega_{\max} = 530\ \mathrm{cm}^{-1}$ (65 meV) correspond to bulk Si phonons, in accordance with the Debye frequency of Si(100). A second group of collective motions, the red shaded area in Fig. 14, represents the Si—H bending modes between 580 and 650 cm^{-1}. The Si—H system mode for (b) has been identified in our recent work [26]. The phonon spectrum of (b) together with the Si—H system mode energy and the largest bulk phonon mode $\omega_{\max}$ is also shown in Fig. 14.

The vector $\mathbf{e}_q$, which serves as the degree of freedom for the system mode q and is used in the subsequent calculation of the system-bath coupling elements, is set up in the following way: the $3N$ components representing the system motion are restricted to atoms with displacements of at least 5% of the maximum displacement, all the other entries are set to zero. This is done to avoid an artificially large coupling due to the finite cluster sizes. In order to ensure orthogonality between the system-mode

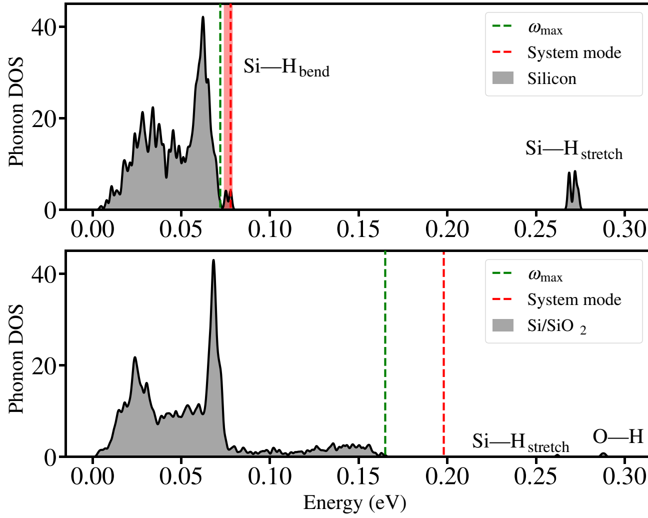

FIG. 14. Phonon spectrum together with the corresponding system-mode energies for (a) H-passivated Si(100) surface (upper panel) and (b) a Si/SiO_2 interface system (lower panel). The results are obtained using the classical force-field ReaxFF.

vector $\mathbf{e}_q$ and the environment modes $\mathbf{e}_Q$, we select $3N-1$ random $3N$-dimensional vectors $\mathbf{u}_i$, orthogonalized the system $(\mathbf{e}_q, \mathbf{u}_i)$, and constructed a $(3N-1)\times 3N$ transformation matrix $\mathbf{U}$ using the orthogonalized vectors $\mathbf{u}_i$. The matrix $\mathbf{U}$ is further used to transform the $3N \times 3N$ Hessian $\mathbf{H} = (\partial V/\partial\mathbf{x}\partial\mathbf{x})|_0$ into a constrained (a subspace orthogonal to the system mode) $(3N-1)\times(3N-1)$ Hessian given by

$$\mathbf{H}' = \mathbf{U}\mathbf{H}\mathbf{U}^T, \tag{C5}$$

which upon diagonalization yields $3N-1$ constrained bath normal modes $\mathbf{e}'_Q$, each of length $3N-1$. Using the inverse transformation

$$\mathbf{e}_Q = \mathbf{U}^T\mathbf{e}'_Q, \tag{C6}$$

finally gives $3N-1$ bath-mode vectors with a length of $3N$. This approach guarantees one anharmonic system mode, represented by $\mathbf{e}_q$, and $3N-1$ harmonic bath modes, $\mathbf{e}_Q$, all being orthogonal to each other, $\mathbf{e}_{Q_i}\mathbf{e}_{Q_j} = \delta_{i,j}$ and $\mathbf{e}_{Q_i}\mathbf{e}_q = 0$.

All linear and quadratic coupling terms are calculated using a classical ReaxFF force field [78] implemented in the LAMMPS code [112]. We conduct the calculations along the anharmonic system DOF $\mathbf{e}_q$ at 31 displacements $\mathbf{q} = q\mathbf{e}_q$ within the interval $[-0.75, +0.75]a_0\sqrt{m}$, which is sufficient to cover at least the lowest eigenstates. The final results for both studied systems, (a) Si—H bending on a surface and (b) Si—H breakage at a Si/SiO_2 interface, are summarized in Table II. One can clearly see that the total lifetime τ_1^{total} for (a) and (b) is dominated by a two-phonon relaxation process, which is intuitive to understand following that the energies of both system modes are greater than the largest bulk mode, $\omega_{\text{system}} > \omega_{\max}$. One-phonon transition rates are orders of magnitude smaller due to the small broadening value γ, which is set to 0.1 cm^{-1} for both calculations. Hence, these energy forbidden transitions, are effectively suppressed in our perturbation theory approach. The parameter γ, however, can only be chosen in an empirical way. In previous studies its value has been related to the mean energy level spacing of the phonon bath [77,79], which in our study is around approximately 0.3 cm^{-1}. Nevertheless, the dependence of the lifetime $\tau_1(\gamma)$ on the broadening width γ shows a nonmonotonous behavior, as can be seen in Fig. 15, rendering it difficult to derive a reasonable criterion for this parameter. We further motivate our choice of $\gamma = 0.1$ cm^{-1} by comparing our result for the Si—H bending mode lifetime of 793 fs to previous studies [77,79] which suggest $\tau_1 = 1600$ fs. To overcome the shortcomings of Fermi's golden rule one would have to go beyond the perturbation theory approach used here, which is outside of the scope of this work.

Further insight into the dissipation mechanism can be gained by analyzing the two-phonon process in detail. Therefore, Fig. 16 shows the individual contribution of

TABLE II. Calculated vibrational lifetimes (τ_1^{total}, $\tau_1^{(1)}$, and $\tau_1^{(2)}$) together with the corresponding rates ($\Gamma_{1,0}^{(1)}$, $\Gamma_{1,0}^{(2a)}$, and $\Gamma_{1,0}^{(2b)}$) for the first excited system mode of the H-passivated Si surface (a) and the Si/SiO_2 system (b) and two different temperatures (in brackets are the upward rates). The units for the Si—H_{bend} mode rates is ps^{-1}, while the ns^{-1} is used for Si—H_{break}. Note the good agreement for the Si—H bending mode with well-established values in the literature [74,77,79]. The last line shows the one- and two-phonon rates and lifetime calculated for the Si—H_{break} mode for the $2 \to 1$ transition.

Mode	T (K)	τ_1^{total} (ps)	$\Gamma_{1,0}^{(1)}$ ($\text{ps}^{-1}/\text{ns}^{-1}$)	$\tau_1^{(1)}$ (ps)	$\Gamma_{1,0}^{(2a)}$ ($\text{ps}^{-1}/\text{ns}^{-1}$)	$\Gamma_{1,0}^{(2b)}$ ($\text{ps}^{-1}/\text{ns}^{-1}$)	$\tau_1^{(2)}$ (ps)
Si–H_{bend}	0	0.793	1.28×10^{-3}	775.29	1.259	7.45×10^{-5}	0.793
Si(100)	300	0.572	2.49×10^{-3}	601.09	1.743	1.05×10^{-4}	0.573
			(8.29×10^{-4})		(3.78×10^{-5})	(3.79×10^{-6})	
Si—H_{break}	0	218.33	2.44×10^{-3}	4.09×10^5	4.571	6.00×10^{-3}	218.45
(Si/SiO_2)	300	190.59	2.59×10^{-3}	3.95×10^5	5.237	6.45×10^{-3}	190.69
			(6.53×10^{-5})		(6.61×10^{-6})	(1.45×10^{-6})	
Si—$H_{\text{break}}^{2\to 1}$	0	80.165	6.23×10^{-3}	1.60×10^5	12.432	0.035	80.20

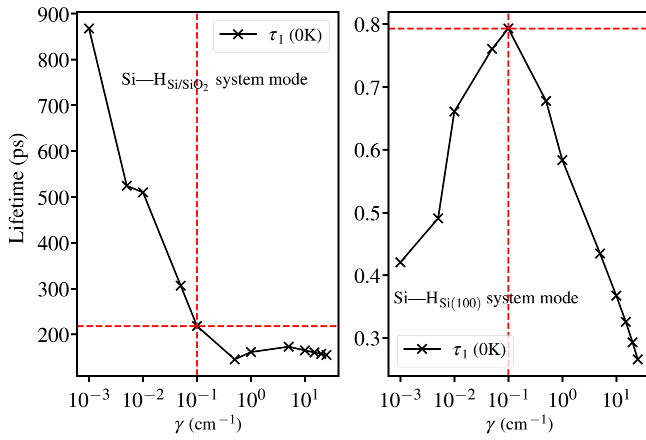

FIG. 15. The lifetime τ_1 for both systems studied here as a function of the broadening parameter γ. This parameter represents a Lorentzian and replaces the Dirac δ function in Fermi's golden rule for the numerical calculations.

phonon pairs $\{\omega_k, \omega_l\}$ within a two-dimensional histogram with a bin size of 5 cm^{-1} $\times$ 5 cm^{-1}. One can see from the upper panel, which corresponds to the Si–surface system (a), that the energy is transferred along the diagonal $\hbar\omega_k + \hbar\omega_l = \Delta E_{1,0}$, as to be expected, with the largest contribution comprising one low- and one high-energy phonon in the range of 21–26 meV and 52–57 meV. Furthermore, also ratios of $\omega_k/\omega_l \sim 1/6, 1/1.5$ yield non-negligible contributions to the total rate $\Gamma^{(2)}_{1,0}$, whereas $\omega_k/\omega_l \sim 1/1$ ($\Gamma^{(2b)}_{1,0}$) only plays a minor role. On the other hand, for the Si—H system mode at a Si/SiO_2 interface (b), shown in the lower panel of Fig. 16 the dissipation pathway via two similar phonons ($\omega_k \sim \omega_l$) is more pronounced, see also Table II. As an alternative, again two phonons, which in total fit $\Delta E_{1,0}$ can be seen in Fig. 16.

As already outlined in Sec. III, ideally it would be possible to calculate lifetimes for all vibrationally excited states for the system-mode potential using the approach described here. However, for the problem at hand, the next vibrational state yields $\Delta E_{2,0} > 2\hbar\omega_{\max}$, which would require a three-phonon process and is thus outside of our model. Instead, we use a harmonic approximation and allow only for neighboring transitions $\Delta n = \pm 1$ with a simple linear scaling law $\Gamma^{\downarrow}_{i,i-1} = i\Gamma^{\downarrow}_{1,0}$. Such a simple model was proposed and used in several theoretical models [42,74,80] and shows reasonable agreement with accurate calculations even for anharmonic system modes. In order to estimate the introduced error and further motivate this approximation, we also calculate the one- and two-phonon rates and lifetimes for the 2 $\rightarrow$ 1 transition, see Table II. Since the energy difference $\Delta E_{2,1}$ is still outside the phonon band, $\Gamma^{(2)}_{2,1}$ again dominates the resulting lifetime. Furthermore, we believe that the direct transition 2 $\rightarrow$ 0 is less relevant, due to the fact that at least three bath modes are necessary to dissipate the energy.

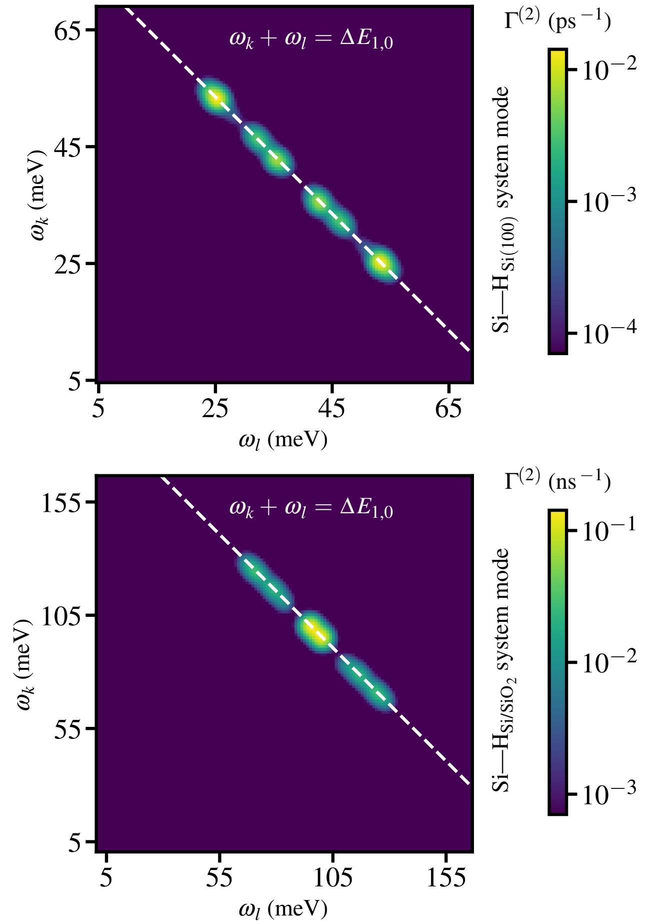

FIG. 16. Composition of the transition rate $\Gamma^{(2),\downarrow}_{1,0}$ for pairs of phonons $\{\omega_k, \omega_l\}$ with a bin size of 5 cm^{-1} $\times$ 5 cm^{-1}. The upper panel shows the two–phonon dissipation for the Si—H bending mode (a), and the lower panel the Si—H breaking system mode at the Si/SiO_2 interface (b), respectively.

Finally, one can see in Table II that the resulting lifetime of $\tau_2 = 80.1$ ps agrees well with the simple model prediction of $\tau_2 = \tau_1/2 = 109.1$ ps.

APPENDIX D: DIPOLE EXCITATIONS

Application of an electric field can have manifold implications onto the dissociation behavior of a chemical bond. First, an external electric field can indeed change the bond potential as well as the bonding strength. Such effects are of particular relevance for STM experiments where field strengths typically reach values of 1 V/Å [40,41,119]. Moreover, it was shown in a recent study that even in electronic devices, where much lower fields are present (approximately 10 MV/cm = 0.1 V/Å), defect creation mechanisms can be substantially affected [120]. Furthermore, an electric field can directly act upon the vibrational states and induce excitations. The field generated by moving electrons couples to the dipole moment $\boldsymbol{\mu}$ of the bond

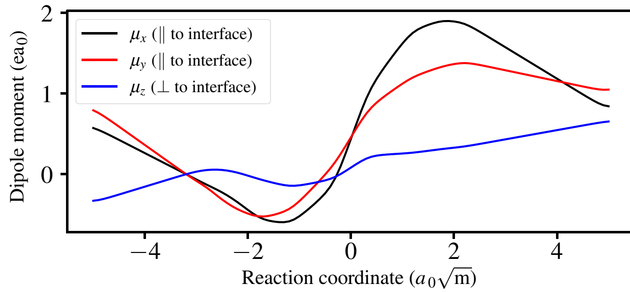

FIG. 17. Components of the dipole moment vector $\boldsymbol{\mu}$ along the reaction coordinate. Components μ_x and μ_y are parallel to the Si/SiO_2 interface, while μ_z is perpendicular to the interface.

and triggers transitions between the vibrational eigenstates. In order to determine the effect of the field on the bonding and the contribution of dipole-induced excitations, the dipole moment vector $\boldsymbol{\mu}$ along the dissociation path must be known.

As shown in Ref. [120], one can approximate the dipole moment vector and its components along the reaction coordinate also from zero-field calculations. Following this approach by defining an effective dipole moment $\boldsymbol{\mu}_{\mathrm{eff}} = \boldsymbol{\mu}_{\mathrm{init}} - \boldsymbol{\mu}_{\mathrm{trans}}$, which is defined as the difference between the initial $\boldsymbol{\mu}_{\mathrm{init}}$ and transition state $\boldsymbol{\mu}_{\mathrm{trans}}$ dipole moment, the change of potential due to an applied field is given by $\Delta E = -\boldsymbol{\mu}_{\mathrm{eff}} \cdot \mathbf{E}$. The results for the x, y, and z component along the reaction path are shown in Fig. 17.

In order to account for static fields during normal operation of a MOSFET, we use the calculated electric field vector at the channel-oxide interface using our TCAD tools. The results of the device simulations for both, the nMOS and the pMOS at the worst-case stress conditions, are given in Fig. 18. As one can see, the field $\mathbf{F}$ is mainly

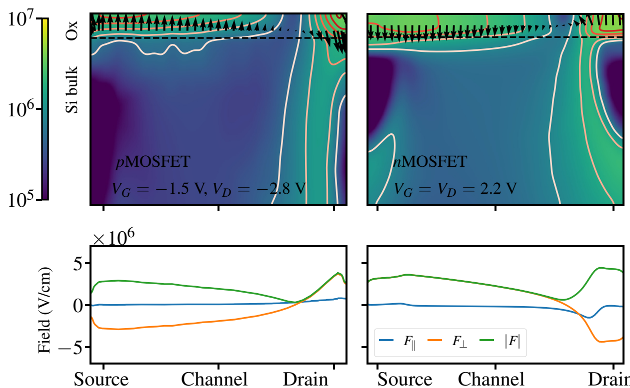

FIG. 18. The electric field within the MOSFET device structures (upper panels) and directly at the channel-oxide interface (lower panels) for the worst-case stress conditions. One can see that the electric field is mainly perpendicular to the interface with field strengths around 5 MV/cm, which does not affect the Si—H bond characteristics.

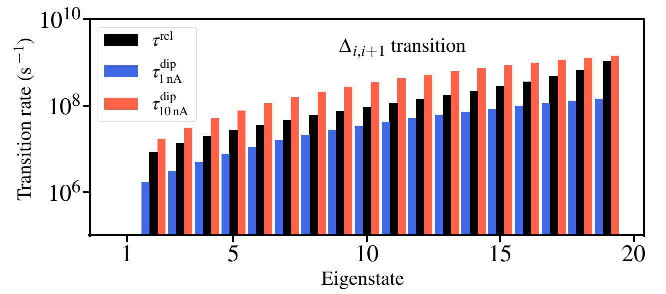

FIG. 19. Comparison of dipole-induced upward rates $\Gamma^{\mathrm{dip}}_{i,f}$ (red and blue bars) and vibrational upward rates $\Gamma^{\mathrm{vib}}_{i,f}$ (black bars) for direct neighboring transitions $\Delta_{n,n+1}$. Only at a high current density with carriers being in equilibrium this process is dominant, however plays only a minor role in the degradation characteristics, see Fig. 10.

oriented perpendicular to the interface and the maximum field strength is around approximately 5 MV/cm, leading to a reduction of the transition barrier of less than 0.05 eV. Hence, the bonding potential in the ground state $V(q)$ is virtually unaffected and its change can be neglected within our calculations.

Furthermore, the calculated current density in the channel region of the devices in conjunction with the dipole moment components $\mu_\parallel$ are used to estimate the contribution of the dipole-induced excitation rates caused by the current density in a MOSFET. We calculate the transition rates $\Gamma^{\mathrm{dip}}_{i,f}$ using Eq. (16) for different currents and compare them to the vibrational upwards rates $\Gamma^{\mathrm{vib}}_{i,f}$ at $T = 300$ K, see Fig. 19. Current densities in scaled MOSFETs already exceed 100 $\mathrm{nA/nm^2}$, which is of a similar order as tunneling currents in Si—H related STM experiments (1–10 nA), assuming that the STM electron beam is of atomic dimensions. One can see that only at higher currents the upward rates for $\Delta n = +1$ are mainly determined by dipole-induced scattering at $T = 300$ K. Although Fig. 19 shows a non-negligible contribution of $\Gamma^{\mathrm{dip}}_{i,f}$, the relevance of dipole-induced excitations is limited in hot-carrier-related device reliability issues. Only at the source side, where carriers are still close to equilibrium but a high current density is present, they play a minor role, see Fig. 10. However, starting from the middle of the channel, carriers have already gained enough energy to scatter into the available resonance, which dominates the upward transitions with typical values of Γ^{res} between 10^9 and 10^{10} s^{-1}.

[1] T. Grasser, M. Waltl, Y. Wimmer, W. Goes, R. Kosik, G. Rzepa, H. Reisinger, G. Pobegen, A. M. El-Sayed, A. Shluger, and B. Kaczer, in *2015 IEEE International Electron Devices Meeting (IEDM)* (2015), p. 20.1.1.

[2] T. Grasser, M. Waltl, K. Puschkarsky, B. Stampfer, G. Rzepa, G. Pobegen, H. Reisinger, H. Arimura, and B. Kaczer, in *2017 IEEE International Reliability Physics Symposium (IRPS)* (2017), p. 6A–2.1.
[3] A. T. Krishnan, S. Chakravarthi, P. Nicollian, V. Reddy, and S. Krishnan, Negative bias temperature instability mechanism: The role of molecular hydrogen, Appl. Phys. Lett. **88**, 153518 (2006).
[4] J. H. Stathis, S. Mahapatra, and T. Grasser, Controversial issues in negative bias temperature instability, Microelectron. Reliability **81**, 244 (2018).
[5] M. Bina, S. Tyaginov, J. Franco, K. Rupp, Y. Wimmer, D. Osintsev, B. Kaczer, and T. Grasser, Predictive hot-carrier modeling of *n*-Channel MOSFETs, IEEE Trans. Electron Devices **61**, 3103 (2014).
[6] S. Tyaginov, M. Jech, J. Franco, P. Sharma, B. Kaczer, and T. Grasser, Understanding and modeling the temperature behavior of hot-carrier degradation in SiON nMOSFETs, IEEE Electron Device Lett. **37**, 84 (2016).
[7] C. Guerin, V. Huard, and A. Bravaix, General framework about defect creation at the Si/SiO_2 interface, J. Appl. Phys. **105**, 114513 (2009).
[8] A. Bravaix, C. Guerin, V. Huard, D. Roy, J. M. Roux, and E. Vincent, in *2009 IEEE International Reliability Physics Symposium* (2009), p. 531.
[9] A. Bravaix, Y. M. Randriamihaja, V. Huard, D. Angot, X. Federspiel, W. Arfaoui, P. Mora, F. Cacho, M. Saliva, C. Besset, S. Renard, D. Roy, and E. Vincent, in *2013 IEEE International Reliability Physics Symposium (IRPS)* (2013), p. 2D.6.1.
[10] S. Novak, C. Parker, D. Becher, M. Liu, M. Agostinelli, M. Chahal, P. Packan, P. Nayak, S. Ramey, and S. Natarajan, in *2015 IEEE International Reliability Physics Symposium* (2015), p. 2F.2.1.
[11] W. Gös, Y. Wimmer, A.-M. El-Sayed, G. Rzepa, M. Jech, A. Shluger, and T. Grasser, Identification of oxide defects in semiconductor devices: A systematic approach linking DFT to rate equations and experimental evidence, Microelectron. Reliability **87**, 286 (2018).
[12] J. T. Krick, P. M. Lenahan, and G. J. Dunn, Direct observation of interfacial point defects generated by channel hot hole injection in n-channel metal oxide silicon field effect transistors, Appl. Phys. Lett. **59**, 3437 (1991).
[13] P. M. Lenahan, What can electron paramagnetic resonance tell us about the Si/SiO_2 system?, J. Vac. Sci. **16**, 2134 (1998).
[14] P. Lenahan, Atomic scale defects involved in MOS reliability problems, Microelectron. Eng. **69**, 173 (2003).
[15] J. P. Campbell and P. M. Lenahan, Density of states of $Pb_1 Si/SiO_2$ interface trap centers, Appl. Phys. Lett. **80**, 1945 (2002).
[16] A. Stesmans, B. Nouwen, and V. Afanas'ev, Interface defect in thermal hyperfine interaction, Phys. Rev. B - Condens. Matter Mater. Phys. **58**, 15801 (1998).
[17] C. Hu, S. C. Tam, F.-C. Hsu, P.-K. Ko, T.-Y. Chan, and K. W. Terrill, Hot-electron-induced MOSFET degradation-model, monitor, and improvement, IEEE Trans. Electron Devices **32**, 375 (1985).
[18] B. S. Doyle, M. Bourcerie, C. Bergonzoni, R. Benecchi, A. Bravis, K. R. Mistry, and A. Boudou, The generation and characterization of electron and hole traps created by hole injection during low gate voltage hot-carrier stressing of n-MOS transistors, IEEE Trans. Electron Devices **37**, 1869 (1990).
[19] S. E. Rauch and G. La Rosa, The energy-driven paradigm of nMOSFET hot-carrier effects, IEEE Trans. Device Mater. Reliability **5**, 701 (2005).
[20] K. Hess, L. Register, B. Tuttle, J. Lyding, and I. Kizilyalli, Impact of nanostructure research on conventional solid-state electronics: The giant isotope effect in hydrogen desorption and CMOS lifetime, Physica E: Low-Dimens. Syst. Nanostruct. **3**, 1 (1998).
[21] K. Hess, A. Haggag, W. McMahon, B. Fischer, K. Cheng, J. Lee, and J. Lyding, in *2000 IEEE International Electron Devices Meeting (IEDM)* (2000), p. 93.
[22] W. McMahon and K. Hess, A multi-carrier model for interface trap generation, J. Comput. Electron. **1**, 395 (2002).
[23] W. McMahon, A. Haggag, and K. Hess, Reliability scaling issues for nanoscale devices, IEEE. Trans. Nanotechnol. **2**, 33 (2003).
[24] A. Makarov, S. E. Tyaginov, B. Kaczer, M. Jech, A. Chasin, A. Grill, G. Hellings, M. I. Vexler, D. Linten, and T. Grasser, in *2017 IEEE International Electron Devices Meeting (IEDM)* (2017), p. 13.1.1.
[25] M. Jech, S. E. Tyaginov, B. Kaczer, J. Franco, D. Jabs, C. Jungemann, M. Waltl, and T. Grasser, in *2019 IEEE International Electron Devices Meeting (IEDM)* (2019), p. 24.1.1.
[26] M. Jech, A.-M. El-Sayed, S. Tyaginov, A. L. Shluger, and T. Grasser, *Ab Initio* treatment of silicon-hydrogen bond rupture at Si/SiO" interfaces, Phys. Rev. B **100**, 195302 (2019).
[27] P. Saalfrank, Quantum dynamical approach to ultrafast molecular desorption from surfaces, Chem. Rev. **106**, 4116 (2006).
[28] A. Stesmans, B. Nouwen, and V. V. Afanasev, Pb_1 interface defect in thermal (100)Si/SiO_2: 29Si hyperfine interaction, Phys. Rev. B **58**, 15801 (1998).
[29] V. V. Afanas'ev and A. Stesmans, Thermally induced Si(100)/SiO_2 interface degradation in Poly-Si/SiO_2/Si structures: Evidence for a hydrogen-stimulated process, J. Electrochem. Soc. **148**, G279 (2001).
[30] H. Raza, Theoretical study of isolated dangling bonds, dangling bond wires, and dangling bond clusters on a H:Si (001)-(2 × 1) surface, Phys. Rev. B **76**, 045308 (2007).
[31] A. Stesmans and V. V. Afanas'ev, Electrical activity of interfacial paramagnetic defects in thermal (100)Si/SiO_2, Phys. Rev. B **57**, 10030 (1998).
[32] E. H. Poindexter, P. J. Caplan, B. E. Deal, and R. R. Razouk, Interface states and electron spin resonance centers in thermally oxidized (111) and (100) silicon wafers, J. Appl. Phys. **52**, 879 (1981).
[33] K. Kato, T. Yamasaki, and T. Uda, Origin of Pb_1 center at SiO_2/Si(100) interface: First-principle calculations, Phys. Rev. B **73**, 073302 (2006).
[34] M. Rohrmüller, W. G. Schmidt, and U. Gerstmann, Electron paramagnetic resonance calculations for hydrogenated Si surfaces, Phys. Rev. B **95**, 125310 (2017).
[35] U. Gerstmann, M. Rohrmüller, F. Mauri, and W. Schmidt, Ab initio *g*-tensor calculation for paramagnetic surface

states: Hydrogen adsorption at Si surfaces, Phys. Status Solidi c **7**, 157 (2010).
[36] A. J. Mayne and D. Riedel, Electronic control of single-molecule dynamics, Chem. Rev. **106**, 4355 (2006).
[37] A. J. Mayne, D. Riedel, G. Comtet, and G. Dujardin, Atomic-scale studies of hydrogenated semiconductor surfaces, Prog. Surf. Sci. **81**, 1 (2006).
[38] K. Stokbro, C. Thirstrup, M. Sakurai, U. Quaade, B. Hu, F. Perez-Murano, and F. Grey, STM-Induced Hydrogen Desorption via a Hole Resonance, Phys. Rev. Lett. **80**, 2618 (1998).
[39] K. Stokbro, B. Y.-K. Hu, C. Thirstrup, and X. C. Xie, First-principles theory of inelastic currents in a scanning tunneling microscope, Phys. Rev. B **58**, 8038 (1998).
[40] P. Avouris, R. Walkup, A. Rossi, T.-C. Shen, G. Abeln, J. Tucker, and J. Lyding, STM-induced H atom desorption from Si(100): Isotope effects and site selectivity, Chem. Phys. Lett. **257**, 148 (1996).
[41] P. Avouris, R. Walkup, A. Rossi, H. Akpati, P. Nordlander, T.-C. Shen, G. Abeln, and J. Lyding, Breaking individual chemical bonds via STM-induced excitations, Surf. Sci. **363**, 368 (1996), Dynamical Quantum Processes on Solid Surfaces.
[42] B. Persson and P. Avouris, Local bond breaking via STM-induced excitations: The role of temperature, Surf. Sci. **390**, 45 (1997).
[43] T. C. Shen, Atomic-scale desorption through electronic and vibrational excitation mechanisms, Science **268**, 1590 (1995).
[44] T. C. Shen and P. Avouris, Electron stimulated desorption induced by the scanning tunneling microscope, Surf. Sci. **390**, 35 (1997).
[45] T. C. Shen, J. A. Steckel, and K. D. Jordan, Electron-stimulated bond rearrangements on the H/Si(100)-3 $\times$ 1 surface, Surf. Sci. **446**, 211 (2000).
[46] J. W. Lyding, K. Hess, G. C. Abeln, D. S. Thompson, J. S. Moore, M. C. Hersam, E. T. Foley, J. Lee, S. T. Hwang, H. Choi, and Avouris, Ultrahigh vacuum-scanning tunneling microscopy nanofabrication and hydrogen, Appl. Surf. Sci. **130-132**, 221 (1998).
[47] E. Foley, A. Kam, J. Lyding, and P. Avouris, Cryogenic UHV-STM Study of Hydrogen and Deuterium Desorption from Si (100), Phys. Rev. Lett. **80**, 1336 (1998).
[48] J. Kanasaki, K. Ichihashi, and K. Tanimura, Scanning tunnelling microscopy study on hydrogen removal from Si(001)-(2 $\times$ 1): H surface excited with low-energy electron beams, Surf. Sci. **602**, 1322 (2008).
[49] C. Thirstrup, M. Sakurai, T. Nakayama, and M. Aono, Atomic scale modifications of hydrogen-terminated silicon 2 $\times$ 1 and 3 $\times$ 1 (001) surfaces by scanning tunneling microscope, Surf. Sci. **411**, 203 (1998).
[50] X. Tong and R. A. Wolkow, Electron-induced H atom desorption patterns created with a scanning tunneling microscope: Implications for controlled atomic-scale patterning on H-Si(100), Surf. Sci. **600**, L199 (2006).
[51] K. Cheng, J. Lee, Z. Chen, S. A. Shah, K. Hess, J.-P. Leburton, and J. W. Lyding, Fundamental connection between Hydrogen/Deuterium desorption at silicon surfaces in ultrahigh vacuum and at Oxide/Silicon interfaces in metal-oxide-Semiconductor devices, J. Vac. Sci. **19**, 1119 (2001).
[52] M. Sakurai, C. Thirstrup, T. Nakayama, and M. Aono, Atomic scale extraction of hydrogen atoms adsorbed on Si(001) with the scanning tunneling microscope, Appl. Surf. Sci. **121**, 107 (1997).
[53] N. Itoh and A. M. Stoneham, Treatment of semiconductor surfaces by laser-induced electronic excitation, J. Phys. Condens. Matter **13**, R489 (2001).
[54] T. Vondrak and X.-Y. Zhu, Dissociation of a Surface Bond by Direct Optical Excitation: H-Si(100), Phys. Rev. Lett. **82**, 1967 (1999).
[55] T. Vondrak and X.-Y. Zhu, Direct photodesorption of atomic hydrogen from Si(100) at 157 nm: Experiment and simulation, J. Phys. Chem. B **103**, 4892 (1999).
[56] G. Boendgen and P. Saalfrank, STM-induced desorption of hydrogen from a silicon surface: An open-system density matrix study, J. Phys. Chem. B **102**, 8029 (1998).
[57] L. Soukiassian, A. J. Mayne, M. Carbone, and G. Dujardin, Atomic-scale desorption of H atoms from the Si(100)-2 $\times$ 1:H surface: Inelastic electron interactions, Phys. Rev. B **68**, 035303 (2003).
[58] Morgenstern Karina, Lorente Nicolas, andRieder Karl-Heinz, Controlled manipulation of single atoms and small molecules using the scanning tunnelling microscope, Physica Status Solidi (b) **250**, 1671 (2013).
[59] G. Dujardin, F. Rose, J. Tribollet, and A. J. Mayne, Inelastic transport of tunnel and field-emitted electrons through a single atom, Phys. Rev. B **63**, 081305 (2001).
[60] B. Persson and J. Demuth, Inelastic electron tunnelling from a metal tip, Solid State Commun. **57**, 769 (1986).
[61] S. Selberherr, *Analysis and Simulation of Semiconductor Devices* (Springer-Verlag, Wien - New York, 1984).
[62] T. Grasser, T.-W. Tang, H. Kosina, and S. Selberherr, A review of hydrodynamic and energy-transport models for semiconductor device simulation, Proc. IEEE **91**, 251 (2003).
[63] P. Sharma, S. E. Tyaginov, S. E. Rauch, J. Franco, A. Makarov, M. I. Vexler, B. Kaczer, and T. Grasser, Hot-carrier degradation modeling of decananometer nMOSFETs using the drift-diffusion approach, IEEE Electron Device Lett. **38**, 160 (2017).
[64] S.-M. Hong, A.-T. Pham, and C. Jungemann, *Deterministic Solvers for the Boltzmann Transport Equation* (Springer, Wien, 2011).
[65] M. V. Fischetti and S. E. Laux, Monte carlo analysis of electron transport in small semiconductor devices including band-structure and space-charge effects, Phys. Rev. B **38**, 9721 (1988).
[66] K. Rupp, C. Jungemann, S.-M. Hong, M. Bina, T. Grasser, and A. Jüngel, A review of recent advances in the spherical harmonics expansion method for semiconductor device simulation, J. Comput. Electron. **15**, 939 (2016).
[67] C. Jungemann, A. T. Pham, B. Meinerzhagen, C. Ringhofer, and M. Bollhöfer, Stable discretization of the boltzmann equation based on spherical harmonics, box integration, and a maximum entropy dissipation principle, J. Appl. Phys. **100**, 024502 (2006).
[68] S.-M. Hong and C. Jungemann, A fully coupled scheme for a boltzmann–poisson equation solver based on a spherical harmonics expansion, J. Comput. Eletronics **8**, 225 (2009).

[69] A.-T. Pham, C. Jungemann, and B. Meinerzhagen, in *2006 International Conference on Simulation of Semiconductor Processes and Devices* (2006), p. 361.

[70] C. Jungemann and B. Meinerzhagen, *Hierarchical Device Simulation*, edited by S. Selberherr, Computational Microelectronics (Springer-Verlag, Wien - New York, 2003).

[71] *Minimos-NT User Manual–Release 2018.04.*

[72] *GTS Framework User Manual*, Global TCAD Solutions.

[73] G. Lindblad, On the generators of quantum dynamical semigroups, Commun. Math. Phys. **48**, 119 (1976).

[74] I. Andrianov and P. Saalfrank, Free vibrational relaxation of H adsorbed on a Si(100) surface investigated with the multi-configurational time-dependent hartree method, Chem. Phys. Lett. **433**, 91 (2006).

[75] I. Andrianov and P. Saalfrank, Theoretical study of vibration-phonon coupling of H adsorbed on a Si(100) surface, J. Chem. Phys. **124**, 34710 (2006).

[76] F. Bouakline, F. Lüder, R. Martinazzo, and P. Saalfrank, Reduced and exact quantum dynamics of the vibrational relaxation of a molecular system interacting with a finite-dimensional bath, J. Phys. Chem. A **116**, 11118 (2012).

[77] F. Bouakline, U. Lorenz, G. Melani, G. K. Paramonov, and P. Saalfrank, Isotopic effects in vibrational relaxation dynamics of H on a Si(100) surface, J. Chem. Phys. **147**, 144703 (2017).

[78] J. C. Fogarty, H. M. Aktulga, A. Y. Grama, A. C. T. van Duin, and S. A. Pandit, A reactive molecular dynamics simulation of the silica-water interface, J. Chem. Phys. **132**, 174704 (2010).

[79] U. Lorenz and P. Saalfrank, A novel system-bath hamiltonian for vibration-phonon coupling: Formulation, and application to the relaxation of Si–H and Si-D bending modes of H/D:Si(100)-(2 $\times$ 1), Chem. Phys. **482**, 69 (2017).

[80] K. Zenichowski, T. Klamroth, and P. Saalfrank, Open-system density matrix description of an STM-driven atomic switch: H on Si(100), Appl. Phys. A **93**, 319 (2008).

[81] R. E. Walkup, D. M. Newns, and P. Avouris, Role of multiple enelastic transitions in atom transfer with the scanning tunneling microscope, Phys. Rev. B **48**, 1858 (1993).

[82] R. Walkup, D. Newns, and P. Avouris, Vibrational heating and atom transfer with the STM, J. Electron Spectros. Relat. Phenomena **64**, 523 (1993).

[83] B. Persson and H. Ueba, Theory of inelastic tunneling induced motion of adsorbates on metal surfaces, Surf. Sci. **502**, 18 (2002).

[84] G. P. Salam, M. Persson, and R. E. Palmer, Possibility of coherent multiple excitation in atom transfer with a scanning tunneling microscope, Phys. Rev. B **49**, 10655 (1994).

[85] S. Gao, M. Persson, and B. I. Lundqvist, Theory of atom transfer with a scanning tunneling microscope, Phys. Rev. B **55**, 4825 (1997).

[86] J. W. Gadzuk, Inelastic resonance scattering, tunneling, and desorption, Phys. Rev. B **44**, 13466 (1991).

[87] J. W. Gadzuk, Resonance-assisted, hot-electron-Induced desorption, Surf. Sci. **342**, 345 (1995).

[88] S. Gao, Quantum kinetic theory of vibrational heating and bond breaking by hot electrons, Phys. Rev. B **55**, 1876 (1997).

[89] A. Abe, K. Yamashita, and P. Saalfrank, STM and laser-driven atom switch: An open-system density-matrix study of H/Si(100), Phys. Rev. B **67**, 235411 (2003).

[90] A. Stesmans, Interaction of Pb defects at the (111)Si/SiO_2 interface with molecular hydrogen: Simultaneous action of passivation and dissociation, J. Appl. Phys. **88**, 489 (2000).

[91] A. Stesmans, Dissociation kinetics of hydrogen-passivated P_b defects at the (111)Si/SiO_2 interface, Phys. Rev. B **61**, 8393 (2000).

[92] G. Pobegen, S. Tyaginov, M. Nelhiebel, and T. Grasser, Observation of normally distributed energies for interface trap recovery after hot-carrier degradation, IEEE Electron Device Lett. **34**, 939 (2013).

[93] A. Stesmans, Passivation of Pb_0 and Pb_1 interface defects in thermal (100) Si/SiO_2 with molecular hydrogen, Appl. Phys. Lett. **68**, 2076 (1996).

[94] A. Stesmans, Defect relaxation at the origin of reduction in mobile proton generation at Si/SiO_2/Si interfaces during annealing in H_2, J. Appl. Phys. **94**, 7586 (2003).

[95] P. M. Lenahan and P. V. Dressendorfer, An electron spin resonance study of radiation-induced electrically active paramagnetic centers at the Si/SiO_2 interface, J. Appl. Phys. **54**, 1457 (1983).

[96] N. M. Johnson, C. Herring, and C. G. Van de Walle, Inverted Order of Acceptor and Donor Levels of Monatomic Hydrogen in Silicon, Phys. Rev. Lett. **73**, 130 (1994).

[97] N. H. Nickel, G. B. Anderson, N. M. Johnson, and J. Walker, Nucleation of hydrogen-induced platelets in silicon, Phys. Rev. B **62**, 8012 (2000).

[98] C. Herring, N. M. Johnson, and C. G. Van de Walle, Energy levels of isolated interstitial hydrogen in silicon, Phys. Rev. B **64**, 125209 (2001).

[99] S. T. Pantelides *et al.*, in *Silicon Carbide and Related Materials 2005*, Materials Science Forum, (Trans Tech Publications Ltd, 2006), Vol. 527, p. 935.

[100] L. Tsetseris, S. T. Pantelides, Migration, Incorporation, and passivation reactions of molecular hydrogen at the Si(100)/SiO_2 interface, Phys. Rev. B **70**, 245320 (2004).

[101] L. Tsetseris and S. T. Pantelides, Hydrogenation/Deuteration of the Si-SiO_2 interface: Atomic-scale mechanisms and limitations, Appl. Phys. Lett. **86**, 1 (2005).

[102] K. L. Brower, Kinetics of H_2 passivation of P_b centers at the (111) Si-SiO_2 interface, Phys. Rev. B **38**, 9657 (1988).

[103] M. Vandemaele, K. Chuang, E. Bury, S. Tyaginov, G. Groeseneken, and B. Kaczer, in *2020 IEEE International Reliability Physics Symposium (IRPS)* (2020), p. 1.

[104] J. E. Shelby, Molecular diffusion and solubility of hydrogen isotopes in vitreous silica, J. Appl. Phys. **48**, 3387 (1977).

[105] K. Stokbro, U. J. Quaade, R. Lin, C. Thirstrup, and F. Grey, Electronic mechanism of STM-induced diffusion of hydrogen on Si(100), Faraday Discuss. **117**, 231 (2000).

[106] A. Bravaix, V. Huard, D. Goguenheim, and E. Vincent, in *2011 International Electron Devices Meeting* (2011), p. 27.5.1.

[107] M. C. Wang, Z. Y. Hsieh, C. S. Liao, C. H. Tu, S. Y. Chen, and H. S. Huang, Effective edge width for 65-nm pMOSFETs and their variations under CHC stress, IEEE Electron Device Lett. **32**, 584 (2011).
[108] I. Polishchuk, Y.-C. Yeo, Q. Lu, T.-J. King, and C. Hu, Hot-carrier reliability comparison for pMOSFETs with ultrathin silicon-nitride and silicon-oxide gate dielectrics, IEEE Trans. Device Mater. Reliability **1**, 158 (2001).
[109] J. Franco, B. Kaczer, A. Chasin, E. Bury, and D. Linten, in *2018 IEEE International Reliability Physics Symposium (IRPS)* (2018), p. 5A.1–1.
[110] L. Gao, P. P. Pal, T. Seideman, N. P. Guisinger, and J. R. Guest, Current-driven hydrogen desorption from graphene: Experiment and theory, J. Phys. Chem. Lett. **7**, 486 (2016).
[111] J. VandeVondele, M. Krack, F. Mohamed, M. Parrinello, T. Chassaing, and J. Hutter, Quickstep: Fast and accurate density functional calculations using a mixed Gaussian and plane waves approach, Comput. Phys. Commun. **167**, 103 (2005).
[112] H. Aktulga, J. Fogarty, S. Pandit, and A. Grama, Parallel reactive molecular dynamics: Numerical methods and algorithmic techniques, Parallel Comput. **38**, 245 (2012).
[113] C.-G. Zhan, J. A. Nichols, and D. A. Dixon, Ionization potential, electron affinity, electronegativity, hardness, and electron excitation energy: Molecular properties from density functional theory orbital energies, J. Phys. Chem. A **107**, 4184 (2003).
[114] Q. Wu and T. Van Voorhis, Extracting electron transfer coupling elements from constrained density functional theory, J. Chem. Phys. **125**, 164105 (2006).
[115] B. Kaduk, T. Kowalczyk, and T. Van Voorhis, Constrained density functional theory, Chem. Rev. **112**, 321 (2012).
[116] N. Holmberg and K. Laasonen, Efficient constrained density functional theory implementation for simulation of condensed phase electron transfer reactions, J. Chem. Theory Comput. **13**, 587 (2017).
[117] N. Holmberg and K. Laasonen, Diabatic model for electrochemical hydrogen evolution based on constrained DFT configuration interaction, J. Chem. Phys. **149**, 104702 (2018).
[118] I. Andrianov and P. Saalfrank, Vibrational relaxation rates for H on a Si (10):(2×1) surface : A two-dimensional model, Chem. Phys. Lett. **350**, 191 (2001).
[119] K. Stokbro, Electric field dependent structural and vibrational properties of the Si(100)-H(2*times*1) surface and its implications for STM induced hydrogen desorption, Surf. Sci. **429**, 327 (1999).
[120] A.-M. El-Sayed, M. B. Watkins, T. Grasser, and A. L. Shluger, Effect of electric field on migration of defects in oxides: Vacancies and interstitials in bulk MgO, Phys. Rev. B **98**, 064102 (2018).